Article

Current Biology

The Mechanochemical Cycle of Mammalian Kinesin-2 KIF3A/B under Load

Graphical Abstract

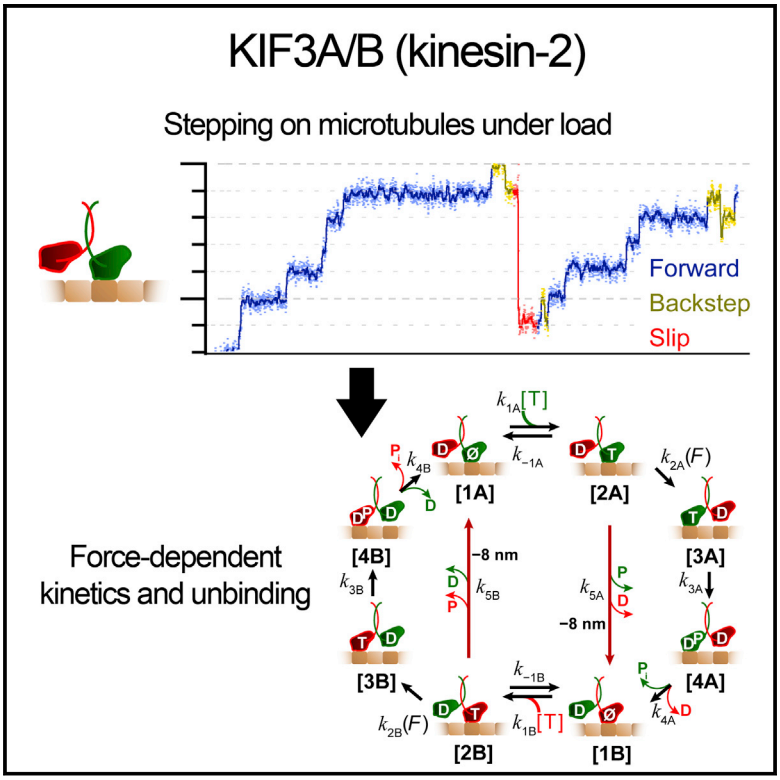

Authors

Johan O.L. Andreasson, Shankar Shastry, William O. Hancock, Steven M. Block

Correspondence

sblock@stanford.edu

In Brief

The responses of motor proteins to external forces determine their net directionality during bidirectional transport. Andreasson et al. use optical trapping to measure the load-dependent kinetics of the kinesin-2 motor KIF3A/B and find that, in contrast to conventional kinesin-1, this motor detaches readily under load.

Highlights

- Kinesin-2 motors behave differently under load from conventional kinesin-1 motors
- KIF3A/B run lengths are highly sensitive to force, and motors can slip under load
- A kinetic cycle derived for KIF3A/B defines the load-dependent kinetic steps
- Behavior under load results from the motor domains, not from the neck linker

Andreasson et al., 2015, Current Biology *25*, 1166–1175
May 4, 2015
http://dx.doi.org/10.1016/j.cub.2015.03.013

CellPress

Current Biology
Article

The Mechanochemical Cycle of Mammalian Kinesin-2 KIF3A/B under Load

Johan O.L. Andreasson,[1,5] Shankar Shastry,[2,6] William O. Hancock,[2,7] and Steven M. Block[3,4,7,*]
[1]Department of Physics, Stanford University, Stanford, CA 94305, USA
[2]Department of Bioengineering, Pennsylvania State University, University Park, PA 16802, USA
[3]Department of Biology, Stanford University, Stanford, CA 94305, USA
[4]Department of Applied Physics, Stanford University, Stanford, CA 94305, USA
[5]Present address: Department of Genetics, Stanford University, Stanford, CA 94305, USA
[6]Present address: Chemistry and Biochemistry Department, University of California, Santa Cruz, Santa Cruz, CA 95064, USA
[7]Co-senior author
*Correspondence: sblock@stanford.edu
http://dx.doi.org/10.1016/j.cub.2015.03.013

SUMMARY

The response of motor proteins to external loads underlies their ability to work in teams and determines the net speed and directionality of cargo transport. The mammalian kinesin-2, KIF3A/B, is a heterotrimeric motor involved in intraflagellar transport and vesicle motility in neurons. Bidirectional cargo transport is known to result from the opposing activities of KIF3A/B and dynein bound to the same cargo, but the load-dependent properties of kinesin-2 are poorly understood. We used a feedback-controlled optical trap to probe the velocity, run length, and unbinding kinetics of mouse KIF3A/B under various loads and nucleotide conditions. The kinesin-2 motor velocity is less sensitive than kinesin-1 to external forces, but its processivity diminishes steeply with load, and the motor was observed occasionally to slip and reattach. Each motor domain was characterized by studying homodimeric constructs, and a global fit to the data resulted in a comprehensive pathway that quantifies the principal force-dependent kinetic transitions. The properties of the KIF3A/B heterodimer are intermediate between the two homodimers, and the distinct load-dependent behavior is attributable to the properties of the motor domains and not to the neck linkers or the coiled-coil stalk. We conclude that the force-dependent movement of KIF3A/B differs significantly from conventional kinesin-1. Against opposing dynein forces, KIF3A/B motors are predicted to rapidly unbind and rebind, resulting in qualitatively different transport behavior from kinesin-1.

INTRODUCTION

The kinesin-2 motor KIF3A/B is an essential protein in mice that is involved in organelle transport and mitosis [1]. The two different motor domains, KIF3A and KIF3B, and a light chain, KAP3, form a heterotrimeric protein complex that is expressed ubiquitously in mammals. KIF3A/B is one of the most abundant kinesin family motors [2], and is particularly enriched in neuronal tissue, where it plays a role in fast axonal transport and axonogenesis [3]. Heterotrimeric kinesin-2 motors are present in diverse organisms, including algae and protozoa, where their functions are often linked to ciliogenesis and intraflagellar transport (IFT) [4]. In higher organisms, ciliopathies resulting from the disruption of IFT are linked to developmental defects and polycystic kidney disease [3, 5].

The effect of mechanical load on kinesin mechanochemistry is best understood for kinesin-1 (conventional kinesin). Optical trapping experiments have shown that kinesin-1 steps processively against hindering loads approaching stall force [6–8], and have provided insights into both the force-dependent kinetic transitions [9] and gating mechanisms by which the ATP hydrolysis cycles of the two motor domains are maintained out of phase to ensure efficient stepping with high processivity [10, 11]. Despite recent investigations into the kinetics [12] and load-dependent performance of different kinesin-2 motors [13, 14], the details of their force-dependent mechanochemistry are lacking. Under loads from a stationary optical trap, the time that *Xenopus* kinesin-2 motors stall before detaching from the microtubule was found to be less than half that of kinesin-1 [14], and *Caenorhabditis elegans* kinesin-2 was found to have shorter run lengths than kinesin-1 at comparable forces [8, 15]. The unloaded processivity of mammalian kinesin-2 was also found to be considerably less than that of kinesin-1, and this reduced processivity could be explained by the longer neck-linker domain of kinesin-2 [16]. Another unresolved question is whether the heterodimeric structure of kinesin-2 plays any role in its load-dependent processivity [15, 17].

Because several kinesin-2 motors are often attached to a single cargo and can interact with kinesin-1, opposing dynein motors, or even myosin [18], understanding their force-dependent behavior is critical for describing their function in living cells. Experiments have been conducted in vitro on teams of identical [19] and opposing motors [20], and models describing cargo transport by multiple motors have been advanced [21–23]. Although such models can capture aspects of the observed transport dynamics, their phase space is large, and the predicted behavior can vary extensively depending upon the choice

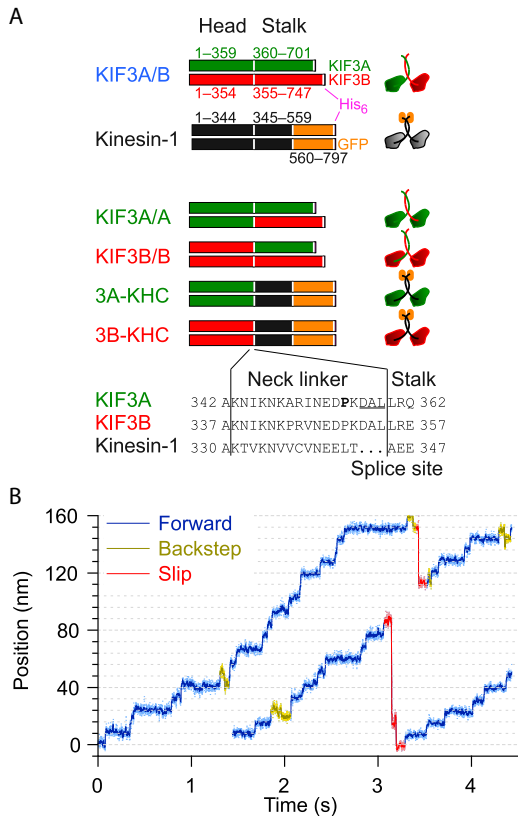

Figure 1. KIF3A/B Stepping against Hindering Load in an Optical Force Clamp

(A) Recombinant kinesin constructs used in the study. KIF3A/B (blue label) consists of the full-length KIF3A (green) and KIF3B (red) sequences fused to a C-terminal His_6 tag (pink). Kinesin-1 (black label) is a truncated *D. melanogaster* KHC construct (black) fused to the GFP sequence (orange) and a His_6 tag. Homodimeric mutants were generated by joining the KIF3A or KIF3B motor domains to the stalks of KIF3A/B or kinesin-1. The splice site was the junction between the neck linker and stalk for the respective motors. Two additional mutants of 3A-KHC were also created: 3A-$KHC_{P>A}$ replaces the KIF3A neck-linker proline (P; bold) with alanine, and 3A-$KHC_{P>A,\Delta DAL}$, which carries the identical mutation, together with a deletion of the three C-terminal neck-linker residues (DAL; underscored).

(B) Representative records of single-molecule movement for KIF3A/B (4 pN hindering load, 5 μM ATP) displaying forward steps of 8 nm (blue), backsteps of 8 nm (olive), and slips of variable distance (red).

of input parameters. Single-molecule investigations have not resolved the question of whether kinesin-1 and kinesin-2 motors respond differently to external loads.

Developing a quantitative understanding of bidirectional transport requires a detailed characterization of the load-dependent stepping dynamics of KIF3A/B and the contribution from each subunit to the function of the holoenzyme. Using optical tweezers equipped with a force clamp applied to mammalian KIF3A/B, we set about addressing the following questions. (1) How do kinesin-2 motors behave under external loads? (2) Are the two heads of kinesin-2 functionally equivalent? (3) What influences do the dimerization domains and neck linkers of kinesin-2 have on the load-dependent properties of the motor? Answering these questions is important for describing the fundamental mechanism by which N-terminal kinesin motors generate force, and for understanding how different kinesin family members may be fine-tuned for specific cellular functions.

RESULTS

Load-Dependent KIF3A/B Stepping Differs from Kinesin-1

To explore the influence of external load on the stepping kinetics of kinesin-2, we used a bead assay and optical trap to study heterodimeric mouse KIF3A/B and homodimeric mutants, comparing their behavior to the well-characterized *Drosophila* kinesin-1 wild-type [17, 24] (Figure 1A). Hereafter, we refer to the motor domains and associated neck linkers of the Kif3a and Kif3b gene products as "A heads" and "B heads," respectively. KIF3A/B refers to the full-length, His-tagged wild-type dimer with both A and B heads. The KIF3A/A and KIF3B/B constructs have the B head substituted with an A head and vice versa, generating motors with identical heads, while retaining the wild-type heterodimeric coiled-coil stalk, as described previously [17].

All three KIF3 constructs gave robust, processive movement at ATP concentrations as low as 100 nM (Figure 1B; Figure S1D). Single-motor conditions were confirmed based on Poisson statistical behavior [25]. Steps measuring 8 nm, the microtubule lattice spacing, were observed under a variety of forces and ATP concentrations (Figure 1B; Figures S1A–S1C, S1E, and S1F), suggesting that kinesin-2 moves in a similar hand-over-hand fashion to kinesin-1.

Kinesin-2 runs were infrequent, but consistent from run to run for all constructs. This intermittent activity was not observed in chimeras where KIF3 motor domains were fused to kinesin-1 coiled-coil domains (see below). Both kinesin-1 and KIF17, a homodimeric kinesin-2 motor, as well as the KIF3A/B ortholog KLP11/20 are known to be autoinhibited by their stalks [15, 26, 27]. Our observations are therefore consistent with a mechanism by which the native KIF3A/B stalk or tail, but not the stalk of kinesin-1, weakly inhibits the KIF3A/B motor domains in a similar manner.

Using force-clamp conditions, the properties of kinesin-2 and kinesin-1 were compared across a wide range of forces and ATP concentrations. The first observation was that the velocity of KIF3A/B was much less affected by hindering loads than kinesin-1 (Figure 2A). This contrast indicates that there are differences in the force-dependent rate constants between the two motor families, which result in a crossover in velocities around 4 pN. To detect any differences in the mechanochemical properties of the two KIF3A/B heads, the force-velocity relationships of KIF3A/A and KIF3B/B homodimers were characterized (Figure 2B). KIF3B/B was slightly faster than KIF3A/A at low load, but was slowed to a greater extent by hindering loads. The ATP dependence of velocity at different loads was also assessed (Figures 2C and 2D). Interestingly, for all conditions, the KIF3A/B velocity was close to the average of the corresponding KIF3A/A and KIF3B/B velocities (Figure 2), indicating that the wild-type heterodimeric KIF3A/B motor may, from a simple kinetic perspective, be considered to be largely the sum of its parts (the A and B heads). This conclusion gained additional support from measurements of the KIF3A/B randomness parameter versus load [29], which was intermediate between that of KIF3A/A and KIF3B/B (Figures 2E and 2F).

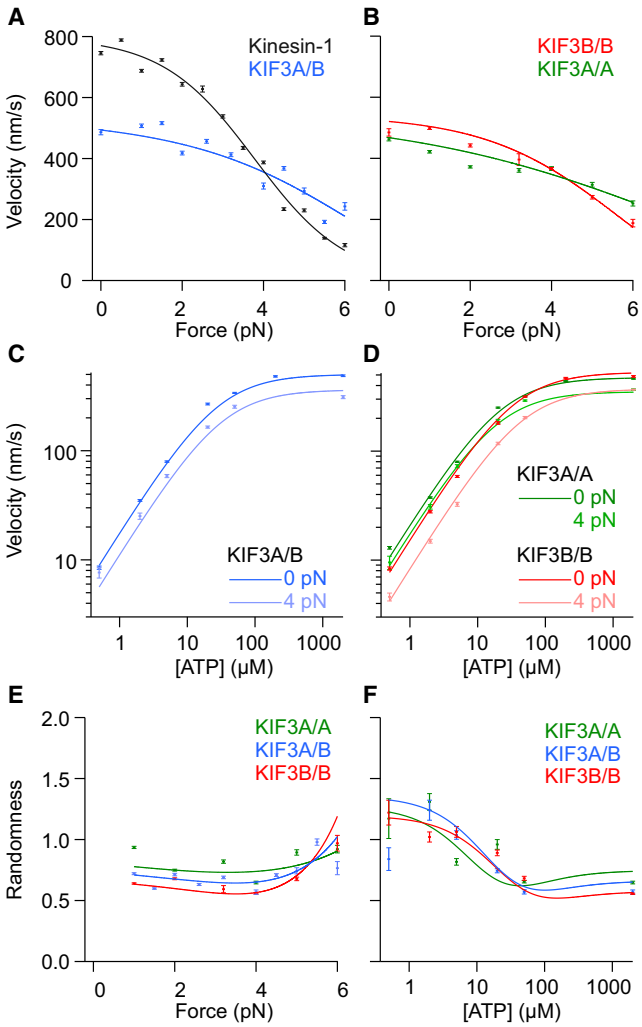

Figure 2. Motor Velocity and Randomness as a Function of Load and ATP

(A and B) Force-velocity curves from force-clamp optical trapping experiments.

(C and D) Velocity at varying ATP concentrations under zero load and 4 pN hindering load.

(E) The randomness parameter, *r*, as a function of force at 2 mM ATP.

(F) The randomness parameter, *r*, as a function of ATP at 4 pN hindering load. Data points and error bars (SEM) indicate experimental velocities or randomness values. Solid curves were derived from a global fit to the data (see Figure 3, Tables S1 and S2, and Supplemental Experimental Procedures). Velocity and randomness results for KIF3A/A in 5 μM ATP are shown in Figures S2A and S2B. Comparisons between KIF3A/B and kinesin-1 randomness versus force or ATP concentration [28] are shown in Figures S2E and S2F.

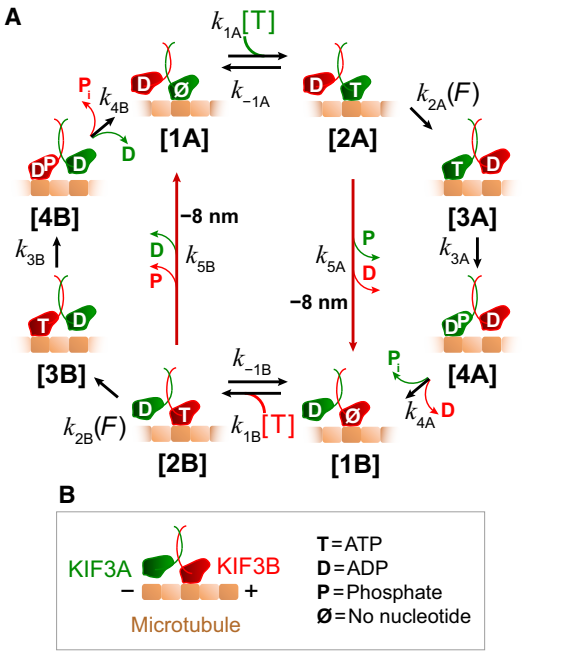

C

Parameter	Transition	KIF3A	KIF3B
k_1	ATP binding	3.06 ± 0.06 $\mu M^{-1}s^{-1}$	2.06 ± 0.03 $\mu M^{-1}s^{-1}$
k_{-1}	ATP unbinding	12 ± 7 s^{-1}	124 ± 10 s^{-1}
k_2	Neck-linker docking	530 ± 21 s^{-1}	1730 ± 211 s^{-1}
k_3	ATP hydrolysis	67.9 ± 0.5 s^{-1}	81.2 ± 0.6 s^{-1}
k_4	P_i release	> 670 s^{-1}	439 ± 26 s^{-1}
k_5	Back-stepping	23.5 ± 0.7 s^{-1}	17 ± 1 s^{-1}
δ	Distance parameter	1.09 ± 0.04 nm	2.28 ± 0.09 nm

Figure 3. Modeling the KIF3A/B Mechanochemical Cycle

(A) Processive stepping pathway for KIF3A/B. Transitions k_{5A} and k_{5B} (dark red arrows) are associated with backsteps.

(B) Legend for the cycle in (A). KIF3A (green) and KIF3B (red) form the KIF3A/B dimer that moves on microtubules (brown).

(C) Table of fit parameters and SEs of fit for the global fit of the kinetic model to the data of Figure 2 and Figures S2A and S2B. Assignments of the mechanochemical transitions that correspond to each rate constant in the pathway are indicated. A three-state model (combining states 3 and 4) was sufficient to model most of the data; however, fitting the model to the randomness data required four states for head B. The data for head A were not sufficient to constrain parameter k_{4A}, so in the actual fit, states 3A and 4A were lumped, equivalent to assuming a very rapid transition [3A] → [4A]. The lower bound for this transition was estimated using FitSpace. Similar model fits were carried out for kinesin-1 and kinesin-2 mutants (Tables S1 and S3).

Model Accounts for Processive Stepping of KIF3A/B under Load

To explore kinetic and mechanical differences between the A and B heads in greater detail, we constructed a combined minimal kinetic pathway for KIF3A/B and used this model to fit the load-dependent velocity and randomness results of Figure 2 and Figures S2A and S2B. Figure 3 shows the mechanochemical cycle for KIF3A/B, which encompasses two 8-nm steps. The corresponding cycle for the KIF3A/A motor was obtained by replacing the states involving the B head cycle ([1B]–[4B]) with those of the A head ([1A]–[4A]), and vice versa for KIF3B/B. All 13 free kinetic parameters (assuming a large fixed value for k_{4A}) were globally fit to the 17 velocity and randomness curves, using the analytical expressions supplied in Supplemental Experimental Procedures. Parameter values are given in Figure 3C, and fits of the model to the data are displayed as solid lines in Figure 2 and Figures S2A and S2B.

As a starting point for the processive stepping cycle, we used the A head in its microtubule-attached, nucleotide-free state ([1A]; this choice is arbitrary). At a given force, the ATP dependence for each construct exhibited Michaelis-Menten-type kinetics. To account for changes in the apparent Michaelis-Menten constant, K_M, with force, we introduced reversible ATP

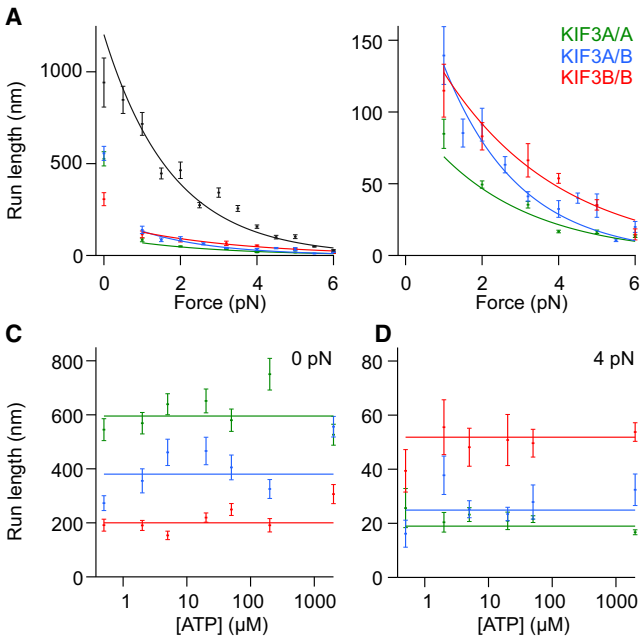

E

	L_{obs} (nm)	L_0 (nm)	δ (nm)
KIF3A/B	380 ± 15	182 ± 30	1.7 ± 0.2
KIF3A/A	595 ± 16	102 ± 8	1.6 ± 0.1
KIF3B/B	200 ± 8	177 ± 22	1.3 ± 0.1
Kinesin-1	942 ± 134	1203 ± 51	2.3 ± 0.1

Figure 4. Dependence of Processivity on Load and ATP

(A) Run length for KIF3 constructs as a function of force, together with kinesin-1 (in dark gray). Mean run lengths (±SE of fit) at each force were calculated from exponential fits to the run-length distribution. Solid curves represent fits to the expression $L = L_0 \exp(-F \cdot \delta / k_B T)$, where L_0 is the run length extrapolated to zero load from hindering-load data and δ is the distance parameter.

(B) KIF3 data from (A) rescaled, showing the differences among motor constructs.

(C and D) ATP dependence of KIF3 run lengths under zero load and 4 pN hindering load. Values are mean ± SE of fit. Solid lines show fits over all ATP levels.

(E) Table of parameters for fits to data in (A) and (B). L_{obs} is the unloaded run length obtained by video tracking, averaged for all ATP concentrations. Run-length results for KIF3A/A in 5 μM ATP and for 6 pN load are displayed in Figures S2C and S2D.

binding, [1A]↔[2A], directly followed by a load-dependent transition, [2A]→[3A] [8]. The forward step of the motor occurs during this transition, and its rate is slowed exponentially under hindering load, according to $k_{2A}(F) = k_{2A,0} \exp(-F \cdot \delta / k_B T)$, where $k_{2A,0}$ is the unloaded rate, δ is a characteristic distance parameter, and $k_B T$ is Boltzmann's constant times the absolute temperature. The next step in the pathway, [3A]→[4A], is ATP hydrolysis, and the final step, [4A]→[1B], consists of attachment and ADP release by the tethered head, followed by phosphate release and detachment by the trailing head, to complete one step [30]. A similar cycle is then repeated by head B.

Occasional backstepping, where the kinesin motor moves 8 nm toward the microtubule minus end, occurs infrequently for kinesin-1, but its frequency can increase significantly when gating (head-head communication) is reduced, for example, by lengthening the neck linker [31]. Backstepping generally exerts only a small effect on velocity (except near the stall force), but it can have a large effect on second-order statistics, such as the randomness parameter [29]. Under 4 pN of hindering load and 5 μM ATP, we observed a 3% probability of backstepping for kinesin-1, consistent with previous observations, and a 6% backstepping probability (N = 1,504) for KIF3A/B (Figure 1B). Backstepping probabilities for the other kinesin-2 constructs were 8% for KIF3A/A (N = 1,206) and 3% for KIF3B/B (N = 1,107).

The high observed randomness values for kinesin-2 (Figures 2E and 2F) could not be modeled using simple kinetic schemes. We therefore introduced backstepping explicitly into the kinetic model as transitions that connect the ATP-bound state to the initial state for the opposite head (dark red arrows for [2A]→[1B] and [2B]→[1A] in Figure 3A). These transitions, with rates k_{5A} and k_{5B}, correspond to 8.2-nm backsteps toward the microtubule minus end. For simplicity, all necessary events in the backstepping subpathway, such as rebinding of the rear head and possible premature ATP hydrolysis that lead to front-head detachment [31], have been lumped into a single rate constant. With the two backstepping transitions incorporated, the global fit of the model to the KIF3A/B data generated backstepping rates that varied with force and ATP and were comparable to the experimental values (e.g., 9% predicted at 4 pN hindering load and 5 μM ATP, versus 6% measured).

Using the experimental data as constraints, the kinetic model of Figure 3 was able to generate satisfactory fits to the force- and ATP-dependent velocity and randomness data of Figure 2. The FitSpace Explorer algorithm [32] was used to confirm that the system was constrained (that is, not underdetermined, and with no fitting parameters subject to large uncertainties); confidence contours and parameters are supplied in Figure S3 and Table S2 and a detailed explanation is given in Supplemental Experimental Procedures. The lower bound for k_{4A} was also estimated using FitSpace. The model represents a reasonable minimal kinetic scheme for KIF3A/B, and highlights salient differences between the hydrolysis cycles of heads A and B.

Kinesin-2 Processivity Is Strongly Force Dependent

The force dependence of processivity is critical to how kinesin-driven intracellular transport will be affected by the actions of opposing motors, or by obstacles within the cell. To determine whether kinesin-2 processivity was maintained against significant opposing forces, we analyzed the load dependence of its run length in a force-clamp assay. Unexpectedly, we found that the processivity of kinesin-2 dropped sharply when a hindering force was applied, such that runs consisted of a mere handful of steps under modest loads (Figure 4; Figures S2C and S2D). Unlike kinesin-1, where run lengths depend only moderately upon load, there were two regimes of processivity for kinesin-2: unloaded and loaded. Unloaded run lengths were fairly long for kinesin-2, approaching those of kinesin-1, but, against any appreciable external load applied by the force clamp (down to a lower limit of ~1 pN), stepping was disrupted and motors lost processivity. To quantify the dependence on force, F, the mean run lengths under hindering load, L, were fit to the exponential expression $L = L_0 \exp(-F \cdot \delta / k_B T)$, where L_0 is the unloaded run length and δ is the distance parameter. Distance parameters were similar for kinesin-1 and kinesin-2, but their run lengths extrapolated to zero load (based on hindering-load

data) differed by nearly an order of magnitude (Figure 4E). Furthermore, the L_0 values derived from fits for kinesin-2 constructs with a KIF3A head were significantly lower than the measured unloaded run length, L_{obs}. This difference reinforces the distinction between the unloaded and loaded regimes, because L_0 and L_{obs} would be expected to be equal if the run length varied continuously across all loads. Under assisting forces, kinesin-2 run lengths were too short to be reliably measured, indicating a significant asymmetry in motor properties with respect to the direction of the applied load.

As with velocity and randomness results, the KIF3A/B run lengths were intermediate between those of KIF3A/A and KIF3B/B under nearly all ATP and load conditions (Figure 4), suggesting that the detachment rate for the heterodimer reflects the additive behavior of its two different motor domains. Unlike a previous report [17], there was no evident ATP dependence on the run length, measured under zero load or 4 pN hindering load (Figures 4C and 4D). The difference is attributable to the improved assay conditions. We also observed transient detachments, followed by reattachments, under hindering loads, hereafter referred to as "slips" (Figure 1B; Figures S1D and S1E). Slips were observed at the end of 28% of runs by KIF3A/B (2 mM ATP, 4 pN hindering load, N = 109). The slipping frequency was similar for KIF3B/B (27%, N = 780) and even higher for KIF3A/A (41%, N = 742). The observed frequency depends upon the run length, because short runs offer a smaller distance over which motors can rebind before the attached bead exits the detection region. The reported difference between KIF3A/A (which has short run lengths under load) and KIF3B/B therefore represents a lower bound. At 5 μM ATP, the slipping frequency was similar for all three constructs (25%–31%, N = 145–305). Slips were also observed for a chimera with KIF3A heads but a kinesin-1 neck and stalk (3A-KHC, 42%, N = 842; described below), but almost no slipping was found with the corresponding KIF3B chimera (3B-KHC, 7%, N = 651), nor for wild-type kinesin-1 (3%, N = 577).

How can one understand the strong load dependence of kinesin-2 processivity in terms of the underlying mechanochemistry? As kinesin takes a forward step, the probability of the motor detaching from the microtubule is determined by a competition between the forward attachment of the unbound tethered head and the dissociation of the bound partner head. The sensitive load dependence of kinesin-2 processivity could therefore be caused by (1) faster dissociation from the one-head-bound state or (2) slower binding of the tethered head under load (or both). To examine the first possibility, we measured the unbinding kinetics of kinesin-1 and kinesin-2 motors subjected to rapid increases in load, as described in the following section. To examine the second possibility, we modified the neck-linker domain, which is predicted to alter the binding kinetics of the tethered head.

Force-Dependent Unbinding Dynamics

By measuring unbinding forces, that is, the forces at which kinesin motors mechanically detach from microtubules, it is possible to probe the load dependence of dissociation in various nucleotide states [33]. To avoid potential artifacts from dimerization domains and to collect sufficient statistics for model fitting, experiments were carried out using the homodimeric chimeras 3A-KHC and 3B-KHC, which consist of KIF3 motor domains and neck linkers fused to a truncated kinesin-1 dimerization domain and stalk (Figure 1A). These motors were previously characterized in single-molecule assays [34]; like full-length KIF3A/B, they step processively along microtubules under load (Figures S1G and S1H). However, their binding efficiency in assays was considerably greater than that of full-length KIF3 constructs, and their kinesin-1-derived stalks removed any concerns about possible differences in elastic compliance when comparing kinesin-2 results with kinesin-1.

The force-dependent unbinding rate, $k_{off}(F)$, can be characterized by the unloaded off rate, k_0, and a distance parameter, δ, according to $k_{off}(F) = k_0 \exp(F \cdot \delta / k_B T)$ [35]. In our experiments, the external load was ramped linearly with time, that is, $F = \alpha t$, where α is the loading rate, in pN s^{-1}. The corresponding unbinding-force distribution was modeled by

$$N(F) = C \exp\left\{\frac{|F|\delta}{k_B T} + \frac{[1 - \exp(|F|\delta / k_B T)]\, k_B T}{\delta \alpha \tau}\right\}, \quad \text{(Equation 1)}$$

where $\tau = 1/k_0$ and C is a constant (adapted from [33]). Parameters k_0 and δ were obtained by fitting the data of Figure 5A.

Unbinding forces were measured in different nucleotide states and for different pulling directions. AMP-PNP (0.5 mM) was used to mimic the ATP state, apyrase (10 U/ml) with no added nucleotide was used to assess the nucleotide-free (apo) state, and ADP (1 mM) was used to assess the ADP state. The apo and ATP states were assayed with a loading rate α = 10 pN s^{-1}, but the fast unbinding in ADP required a much higher loading rate, α = 100 pN s^{-1}.

Some general conclusions can be drawn from the data of Figure 5. First, all kinesin constructs bound quite tightly to the microtubule in the presence of AMP-PNP or no nucleotide. The unbinding rates from these states were significantly lower than the detachment rates determined under similar loads during processive runs (Figure S4), so detachment from these states during processive movement is considered highly unlikely. Second, the unbinding rates in ADP were higher for KIF3A or KIF3B than for kinesin-1, consistent with the shorter run lengths of kinesin-2 motors (Figure 4). Third, the detachment rates in the forward direction in ADP were higher than corresponding rates in the rearward direction. Finally, the load dependence of all detachment rates was very weak (maximum δ = 1.1 nm). Because this load dependence was smaller than the load dependence of the run lengths (Figure 4), the unbinding event itself is unlikely to be the main force-dependent quantity that determines processivity. Put another way, the unbinding rates are correlated with run lengths under load, but these cannot explain the precipitous drop in run length that is observed between unloaded and loaded runs.

The unbinding rates for kinesin-1 in ADP were considerably higher than those previously reported for kinesin-1, which were estimated using a 20-fold lower loading rate [33]. From fits to the backward pulling data (Figure 5B), it can be seen that k_0 is 2- to 3-fold higher for KIF3A and KIF3B than for kinesin-1. Significant asymmetry in the detachment rate between forward and backward pulling has been reported previously for kinesin-1 [33], and it is found here to be a feature of kinesin-2 as well. Using separate unloaded detachment rates for each direction resulted in significantly better fits to the measured distributions (reduced χ^2 = 1.0; kinesin-1 in ADP) compared with a single variable (reduced χ^2 = 3.3).

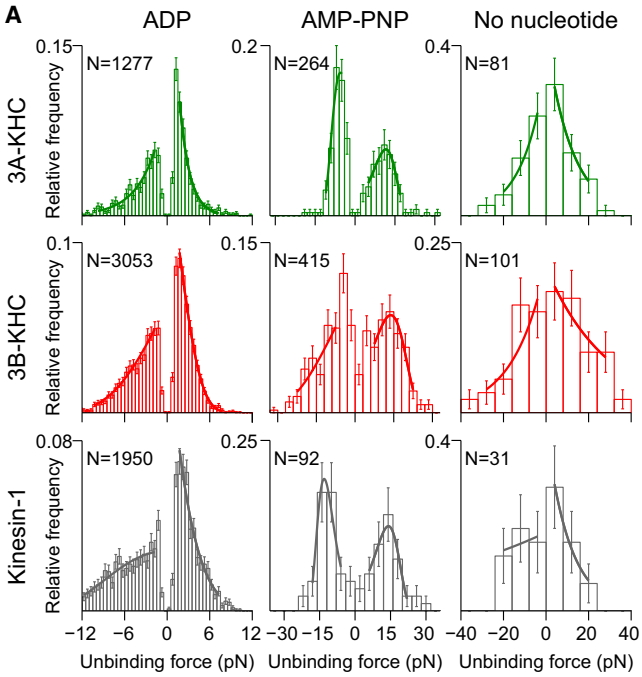

B

Nucleotide	Construct	Backward pulling k_0 (s^{-1})	Backward pulling δ (nm)	Forward pulling k_0 (s^{-1})	Forward pulling δ (nm)
ADP	3A-KHC	33 ± 5	0.0 ± 0.3	69 ± 4	0.9 ± 0.02
	3B-KHC	21 ± 2	0.4 ± 0.1	38 ± 3	0.8 ± 0.1
	Kinesin-1	11 ± 1	0.4 ± 0.1	36 ± 5	0.3 ± 0.2
AMP-PNP	3A-KHC	0.6 ± 0.3	1.1 ± 0.3	0.17 ± 0.06	0.9 ± 0.2
	3B-KHC	0.7 ± 0.3	0.2 ± 0.2	0.18 ± 0.06	0.6 ± 0.1
	Kinesin-1	0.07 ± 0.04	1.1 ± 0.2	0.13 ± 0.07	0.8 ± 0.2
No nucleotide	3A-KHC	0.9 ± 0.3		0.8 ± 0.3	
	3B-KHC	0.7 ± 0.2		0.3 ± 0.2	
	Kinesin-1	0.1 ± 0.4		0.9 ± 0.4	

Figure 5. Unbinding Force Measurements

(A) Unbinding force histograms for 3A-KHC, 3B-KHC, and kinesin-1 (rows) in 1 mM ADP, 0.5 mM AMP-PNP, or no nucleotide (columns). Data points and error bars (SD) indicate the relative frequency. Negative unbinding forces correspond to pulling kinesin toward the microtubule minus end (the hindering-load direction); positive forces are toward the plus end (assisting load direction). Loading rates: 100 pN s^{-1} for ADP; 10 pN s^{-1} for AMP-PNP and no nucleotide (apyrase). Solid lines represent fits to the data under each curve for each pulling direction. Bins with few counts were excluded as well as data at low forces due to the possibility of missed events.

(B) Fit parameters (±SE of fit) are shown for each construct and experimental condition, using the parameters indicated in Equation 1. k_0 is the unloaded off rate and δ is the characteristic distance parameter. For microtubule dissociation rates during processive stepping, see also Figure S4.

Unbinding rates in AMP-PNP for kinesin-2 and kinesin-1 were similar in the assisting direction, but hindering loads generated much higher unbinding rates for kinesin-2. The corresponding distributions for AMP-PNP displayed clear maxima, indicating relatively strong force dependencies, with distance parameters around 1 nm. In the absence of nucleotides, the average unbinding force ranged between 9 and 16 pN for all constructs. Unlike in the presence of AMP-PNP or ADP, where motors repeatedly re-attached to the microtubule following mechanical unbinding, only a single measurement could be performed per bead under nucleotide-free conditions. The failure of reversible binding

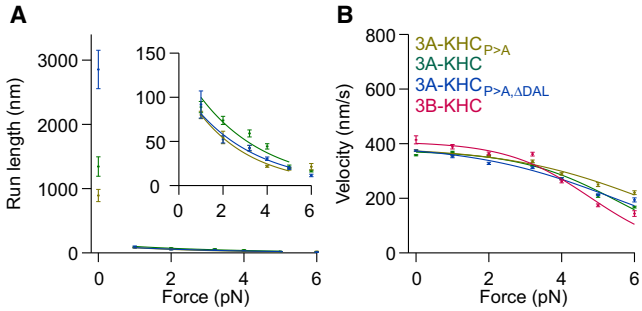

Figure 6. Effect of Neck-Linker Length on Force-Dependent Properties of KIF3

Data are from chimeric constructs consisting of kinesin-2 heads fused to the kinesin-1 stalk (2 mM ATP).

(A) Load dependence of run length for 3A-KHC constructs with different neck-linker domains, along with 3B-KHC, color-coded as in (B). Values at each force are mean ± SE of fit to exponential run-length distributions. Run lengths as a function of force were fit to exponential functions; parameters are given in Table S4. Inset: expanded view of run lengths at nonzero loads.

(B) Load dependence of velocity, colored as shown (legend). Velocity data were fit using a three-state model with a single force-dependent transition. Parameters are given in Table S3. A comparison between velocities and run lengths for homodimers with the native KIF3A/B stalk (KIF3A/A and KIF3B/B) and the kinesin-1 stalk (3A-KHC and 3B-KHC) is shown in Figure S5. The corresponding data for kinesin-1 with an extended neck linker are displayed in Figure S6 and Table S1.

may have been due to the mechanical denaturation of motors lacking bound nucleotide or their detachment from the bead surface. Regardless, the absence of rebinding rendered it unfeasible to collect statistics for the accurate determination of the force sensitivity for detachment (δ). From the limited data available, however, it is clear that detachment rates were low ($k < 1$ s^{-1}) for all constructs.

Differences in Neck-Linker and Neck-Coil Domains Do Not Explain Load-Dependent Processivity

Besides differing in their core catalytic domains, kinesin-1 and kinesin-2 also differ in their neck-linker domains. The kinesin-1 head neck linker consists of 14 residues, whereas the A and B heads of kinesin-2 both have 17-residue neck linkers [16]. Previous work has established that the differences in unloaded processivity between kinesin-1 and -2 likely result from differences associated with their neck linkers and not their core motor domains [16, 34]. Here we tested whether the contrasting load-dependent properties of kinesin-1 and -2 result from differences in neck-linker length or amino acid sequence.

Experiments were conducted to compare the load dependence of the velocity and run length for construct 3A-KHC with construct 3A-KHC$_{P>A}$, which has an effectively longer neck linker, due to swapping out a kinked proline residue [16], and with 3A-KHC$_{P>A,\Delta DAL}$, which has a 14-residue neck linker, similar to kinesin-1 (Figure 1A). The unloaded run lengths depended strongly upon the neck linkers, with 3A-KHC$_{P>A}$ being less, and 3A-KHC$_{P>A,\Delta DAL}$ being considerably more, processive than 3A-KHC (Figure 6A). Quantitatively, these effects were even larger than differences scored previously [16], possibly attributable to using a bead assay for the present experiments, rather than fluorescently tagged motors (beads are less prone to diffuse

away from the microtubule than single proteins). Remarkably, any effects of neck-linker length vanished when force was applied, with all three motors displaying similar run lengths (Figure 6A; Table S4). This finding suggests that even a small external force can disrupt any enhanced gating effects that may result from shortening the neck linker.

Changing the neck-linker length also had no major effect on the velocities of the different 3A-KHC constructs when subjected to either low or high loads (Figure 6B; Table S3). The force-velocity relationship for 3B-KHC was similar to that of 3A-KHC, and the load dependence was slightly weaker than for 3A and 3B homodimers that included the normal kinesin-2 coiled-coil domain (Figure 3; Figure S5; Tables S3 and S4). The run lengths of 3B-KHC were very short for all forces: only a few steps, on average (Figure S5).

We also compared the behavior of kinesin-1 to kinesin-1_{DAL}, which includes the last three residues of the kinesin-2 neck linker inserted between the kinesin-1 neck-linker and neck-coil domains. Extending the kinesin-1 neck linker significantly reduced the unloaded run length and moderately reduced the unloaded velocity, as noted previously [16], but the load dependence was not influenced significantly (Figure S6; Table S1). Hence, the contrasting behavior of kinesin-1 and kinesin-2 under load is not explained by differences in the lengths of their neck linkers.

As a final test, we swapped the neck-linker domains between kinesin-1 and kinesin-2. 3A-KHC with a kinesin-1 neck linker behaved similar to 3A-KHC (data not shown), whereas kinesin-1 with a KIF3A neck linker was not functional. Because neck-linker docking involves interactions with complementary residues in the core motor domain [36], it is not surprising that the linkers are not fully interchangeable. Why the kinesin-2 motor retained function is not clear, but it is possible that specific docking of the neck linker to the core motor domain is necessary for kinesin-1 but not for kinesin-2.

DISCUSSION

The goal of this study was to examine the performance of kinesin-2 family motors under load and to assess the relative contributions of its two different motor domains, along with the neck-linker and stalk domains, to motility. By performing force-clamp measurements using an optical trap, we found unique features that set this family apart from conventional kinesin motors. Under load, the run length of mouse KIF3A/B is sharply reduced, compared to its unloaded run length or to that of kinesin-1 under load. It is also less than half the run length of KLP11/20, the *C. elegans* ortholog [15]. Despite this reduced processivity, however, the velocity of KIF3A/B is much less affected by loads than kinesin-1. The key rate constants that set the stepping rate and processivity therefore have strikingly different load dependencies for kinesin-2 and kinesin-1. By studying homodimeric mutants, we were able to derive a two-head stepping model that fit all the available force-clamp data. The force-velocity and force-run-length curves for KIF3A/B were intermediate between those of KIF3A/A and KIF3B/B, demonstrating that the heterodimer properties could be modeled as an admixture of the behavior of the two motor domains. Furthermore, when fused to a kinesin-1 coiled coil, both KIF3A and KIF3B homodimers were functional, suggesting that the heterodimeric aspect of the kinesin-2 stalk does not play a dominant role in motor mechanics.

By fitting a kinetic scheme of the KIF3A/B mechanochemical cycle to the data, we find that the canonical model for kinesin-1 stepping can be adapted to describe kinesin-2. Kinesin-2 binds strongly to microtubules in its nucleotide-free, ATP-waiting state, and the lack of ATP dependence for the run length indicates that microtubule release takes place from another (distinct) point in the kinetic cycle. When moving against an opposing load, the velocity of KIF3B/B was slowed to a greater extent than KIF3A/A, and the run length of KIF3B/B was reduced to a lesser extent than KIF3A/A. In that sense, the behavior of KIF3B/B was more similar to kinesin-1 than KIF3A/A. In the cycle of Figure 3, the data were best fit by a model in which the load dependence of neck-linker docking for KIF3B (δ for step k_2) is twice that for KIF3A. The structural basis for this difference is not clear, because the neck-linker domains only differ by two residues, neither of which is implicated in key docking interactions with the core catalytic domain and neck cover strand [36].

One hypothesis is that the unconventional load sensitivity of kinesin-2 might be attributable to its longer neck-linker domain. The kinesin step is believed to consist of a concerted conformational change (neck-linker docking) followed by a diffusive component, where the tethered head searches for its next binding site. Thus, a plausible expectation might be that extending the neck linker would bias the ability of the tethered head to find its next microtubule binding site when stepping, particularly under loaded conditions. However, the available data (Figure 6; Figure S5) show that this is not the case: alterations to the neck-linker length and neck-coil domains had negligible effects. Hence, differences in the mechanical properties of kinesin-1 and kinesin-2 reside in the properties of their core motor domains.

No obvious advantage for cellular function emerged from combining two different motor domains, based on comparisons of the velocity and run length of heterodimeric KIF3A/B and the engineered homodimeric constructs, KIF3A/A and KIF3B/B, which all displayed similar behavior. In this respect, mouse kinesin-2 KIF3A/B differs substantially from *C. elegans* kinesin-2 KLP11/20, where the engineered homodimer KLP11/11 (equivalent to KIF3B/B) was reported in a previous study to be 2-fold slower in multiple-motor gliding assays and nonprocessive in single-molecule bead assays [15].

The diminished processivity of kinesin-2 under load could, in principle, result from a greater load dependence of the microtubule affinity, or from a load-dependent increase in the time spent in the low-microtubule-affinity state. To determine whether microtubule affinity was a determining factor, we performed unbinding force experiments. Consistent with the robust processivity observed at low ATP concentrations, kinesin-2 motor domains were strongly bound in the nucleotide-free state. Slow unbinding was also found for heads carrying AMP-PNP, which mimics the ATP-bound state. The off rates under rearward forces in these high-affinity states were greater for kinesin-2 than kinesin-1, but they were significantly lower than the detachment rates when motors stepped against hindering loads at saturating ATP (Figure 5; Figure S4), and therefore cannot account for the observed processivity differences. In the ADP state, the unbinding rates for KIF3A and KIF3B heads were higher than for

kinesin-1, which is broadly consistent with their contrasting run-length behavior. However, the force dependencies for detachment in ADP did not differ significantly between motor families, and were significantly weaker than the force dependence of the run lengths (e.g., δ = 0.4 nm for kinesin-1 unbinding force in ADP versus δ = 1.8 nm for kinesin-1 run length). The load dependence of kinesin-2 processivity cannot therefore be explained simply by differences in the microtubule affinities of various nucleotide states. Instead, the data suggest that the loss of kinesin-2 processivity under load results from the motor spending a greater portion of its hydrolysis cycle in a low-affinity state.

Run-length measurements revealed two distinct regimes of kinesin-2 processivity: loaded and unloaded. Unloaded run lengths were relatively long and strongly influenced by the neck-linker length. By contrast, even at 1 pN (the lowest force explored with the force clamp), run lengths were an order of magnitude shorter and apparently independent of the neck-linker length (Figure 6). This disparity contrasts sharply with kinesin-1, where extensions of the neck linker reduced run lengths to a similar degree from zero load out to loads approaching the stall force (Figure S6). A further distinguishing characteristic of kinesin-2 was its occasional tendency to slip backward, then rapidly reattach to the microtubule and continue stepping (Figure 1B; Figure S1D). Together, these behaviors point toward a mechanism in which motors may spend a portion of the hydrolysis cycle in a weakly bound state that is readily dissociated by external load. Such a weak binding state may share similarities with diffusive mechanisms proposed for processive KIF1A monomers [37]. Alternatively, motors may periodically detach during processive runs, but the presence of an external load may block reattachment in a way not experienced by conventional kinesin. Slipping was observed for the KIF3B/B homodimer and to an even greater degree for the KIF3A/A homodimer and KIF3A motor domains fused to kinesin-1 coiled coils. Because kinesin-1 does not slip, this finding argues against electrostatic tethering by the neck-coil domain as the dominant cause of slipping [38]. Instead, the slipping behavior is more likely attributable to an inherent property of the KIF3A/B motor domains, in particular to KIF3A.

Processive kinesin-2 behavior under load has important implications for understanding bidirectional transport in cells. IFT particles, neuronal vesicles, melanosomes, and other cargoes transported by kinesin-2 also carry dynein, and their overall direction of movement is thought to result from competition between plus- and minus-end-directed motors [4, 18, 39], which may additionally be subject to regulation. Conventional kinesin-1 slows and eventually stalls under increasing hindering loads. Kinesin-2 motors, as we show here, rapidly dissociate under hindering loads, and are able to rebind quickly after slipping backward. Kinesin-2 behavior is therefore more dynamic than kinesin-1. Computational models have shown that the net direction of bidirectional transport and the directional switching rate depend sensitively upon the parameters that describe the load-dependent properties of motors, and particularly upon their detachment rates [22, 23]. The present work supplies a set of quantitative measurements for constraining such models. We note that kinesin-2 run lengths vary nearly exponentially with external load. However, the effective rate of motor dissociation from the microtubule is not similarly exponential, as assumed by at least one model [22]. Instead, the effective dissociation rate is supplied by the motor velocity divided by the run length, and both of these quantities display different load dependence. The kinesin-2 dissociation rate increases steeply with load (Figure S4), making this motor particularly amenable to dynamic switching during bidirectional transport. The residence time of kinesin-1 on the microtubule, by contrast, is predicted to vary minimally under the influence of opposing loads.

EXPERIMENTAL PROCEDURES

Kinesin Constructs

Kinesin constructs were prepared as described [17]. KIF3A/B, KIF3A/A, and KIF3B/B constructs with native stalks terminated by a His_6 tag were expressed in Sf9 cells.

All other constructs were expressed in *Escherichia coli* [16, 34]. The construct described as "kinesin-1" was generated from the *Drosophila melanogaster* kinesin heavy chain (KHC) with a stalk truncated at residue 559, fused to a His-tagged GFP sequence. The remaining constructs all had stalks (residues 345–559) identical to kinesin-1, above. The motor domains and neck linkers for 3A-KHC and 3B-KHC were those from Kif3a and Kif3b, respectively. 3A-$KHC_{P>A}$ and 3A-$KHC_{P>A,\Delta DAL}$ were identical to 3A-KHC, with the exception of a proline-to-alanine substitution in the neck linker (amino acid 355) and, for 3A-$KHC_{P>A,\Delta DAL}$, the deletion of the three last amino acids (DAL) of the neck linker.

Optical Trapping Assay

Optical trapping was carried out as described [31]. For all experiments, the motility buffer was 80 mM PIPES, 1 mM EGTA, 4 mM $MgCl_2$, 2 mg ml^{-1} BSA, 2 mM DTT, 10 μM Taxol (paclitaxel), and nucleotides at the desired concentration. An oxygen-scavenging system (1 mg ml^{-1} glucose, 50 μg ml^{-1} glucose oxidase, and 12 μg ml^{-1} catalase) was added immediately before use. For high-force unbinding experiments in the presence of AMP-PNP or apyrase, higher concentrations of scavenging system were used (5 mg ml^{-1} glucose, 250 μg ml^{-1} glucose oxidase, and 60 μg ml^{-1} catalase). The kinesin molecule was linked to 440-nm-diameter streptavidin-coated polystyrene beads (Spherotech) via a biotinylated Penta-His antibody (QIAGEN). Beads and protein were incubated on a rotator at 4°C for 2 hr or more.

Instrumentation

All data were collected with the instrument described in [40]. For force-clamp experiments, the data were recorded at 20 kHz and decimated to 2 kHz, and the position signal was low-pass filtered at 1 kHz. The force clamp was updated at 500 Hz to maintain a constant offset distance between the trap and bead centers of roughly 80 nm. The laser power was adjusted for each clamp force, and each bead used was calibrated as described [40].

For unbinding force experiments, the trap was maintained at a fixed position, and force was ramped by moving the stage at a constant velocity through the linear region of the trap. Trap stiffness was adjusted appropriately to assure that the bead stayed within this linear region (~120 nm).

Data Analysis

The data were analyzed using IGOR Pro 6.0 (WaveMetrics) to obtain velocities, run lengths, and randomness values for each experimental condition. Velocity distributions were obtained from individual linear fits to kinesin runs (N = 50–700). Each run-length distribution was fit to an exponential distribution, excluding the first bins to account for missing events. The randomness parameter, r, is defined as

$$r = \lim_{t \to \infty} \frac{\langle x(t)^2 \rangle - \langle x(t) \rangle^2}{d\langle x(t) \rangle},$$

where $x(t)$ is motor position, d is the step size, and the angle brackets denote the ensemble average [29]. In all, over 25,000 events were scored in the analysis.

The resulting curves for velocity and randomness, as functions of ATP and force, were fit globally using IGOR Pro: 17 curves for KIF3A/A, KIF3A/B, and KIF3B/B were fit simultaneously to constrain 13 free parameters. The analytical expressions used in the curve fitting were generated in Mathematica 8.0 (Wolfram Research) using methods previously described [31, 41]. The full expressions can be found in Supplemental Experimental Procedures.

The force dependencies of run lengths under hindering loads were fit by exponentials. Because no ATP dependence of run lengths was observed, these data were fit by a constant. For unbinding force measurements, separate fits were performed for the distributions obtained for forward and backward pulling directions (see Results). The characteristic distance, δ, was constrained to be positive.

SUPPLEMENTAL INFORMATION

Supplemental Information includes Supplemental Experimental Procedures, six figures, and four tables and can be found with this article online at http://dx.doi.org/10.1016/j.cub.2015.03.013.

AUTHOR CONTRIBUTIONS

J.O.L.A. devised and performed experiments, analyzed data, and wrote the draft manuscript. S.S. and W.O.H. designed and prepared kinesin constructs. S.M.B. and W.O.H. supplied guidance and edited the manuscript.

ACKNOWLEDGMENTS

We thank Dr. Megan T. Valentine for initiating the study, Dr. Bason E. Clancy for valuable suggestions and help during the initial stages, Alice Shen and Thaddeus Jordan for help with data collection, and Bojan Milic for helpful comments. This work was supported by grants to S.M.B. (5R37GM051453) and W.O.H. (5R01GM076476) from the National Institute of General Medical Sciences of the NIH.

Received: December 15, 2014
Revised: February 13, 2015
Accepted: March 9, 2015
Published: April 9, 2015

REFERENCES

1. Haraguchi, K., Hayashi, T., Jimbo, T., Yamamoto, T., and Akiyama, T. (2006). Role of the kinesin-2 family protein, KIF3, during mitosis. J. Biol. Chem. *281*, 4094–4099.
2. Kondo, S., Sato-Yoshitake, R., Noda, Y., Aizawa, H., Nakata, T., Matsuura, Y., and Hirokawa, N. (1994). KIF3A is a new microtubule-based anterograde motor in the nerve axon. J. Cell Biol. *125*, 1095–1107.
3. Hirokawa, N., and Noda, Y. (2008). Intracellular transport and kinesin superfamily proteins, KIFs: structure, function, and dynamics. Physiol. Rev. *88*, 1089–1118.
4. Cole, D.G. (1999). Kinesin-II, the heteromeric kinesin. Cell. Mol. Life Sci. *56*, 217–226.
5. Lin, F., Hiesberger, T., Cordes, K., Sinclair, A.M., Goldstein, L.S., Somlo, S., and Igarashi, P. (2003). Kidney-specific inactivation of the KIF3A subunit of kinesin-II inhibits renal ciliogenesis and produces polycystic kidney disease. Proc. Natl. Acad. Sci. USA *100*, 5286–5291.
6. Svoboda, K., Schmidt, C.F., Schnapp, B.J., and Block, S.M. (1993). Direct observation of kinesin stepping by optical trapping interferometry. Nature *365*, 721–727.
7. Yildiz, A., Tomishige, M., Vale, R.D., and Selvin, P.R. (2004). Kinesin walks hand-over-hand. Science *303*, 676–678.
8. Schnitzer, M.J., Visscher, K., and Block, S.M. (2000). Force production by single kinesin motors. Nat. Cell Biol. *2*, 718–723.
9. Block, S.M., Asbury, C.L., Shaevitz, J.W., and Lang, M.J. (2003). Probing the kinesin reaction cycle with a 2D optical force clamp. Proc. Natl. Acad. Sci. USA *100*, 2351–2356.
10. Guydosh, N.R., and Block, S.M. (2006). Backsteps induced by nucleotide analogs suggest the front head of kinesin is gated by strain. Proc. Natl. Acad. Sci. USA *103*, 8054–8059.
11. Guydosh, N.R., and Block, S.M. (2009). Direct observation of the binding state of the kinesin head to the microtubule. Nature *461*, 125–128.
12. Albracht, C.D., Rank, K.C., Obrzut, S., Rayment, I., and Gilbert, S.P. (2014). Kinesin-2 KIF3AB exhibits novel ATPase characteristics. J. Biol. Chem. *289*, 27836–27848.
13. Brunnbauer, M., Dombi, R., Ho, T.H., Schliwa, M., Rief, M., and Ökten, Z. (2012). Torque generation of kinesin motors is governed by the stability of the neck domain. Mol. Cell *46*, 147–158.
14. Schroeder, H.W., III, Hendricks, A.G., Ikeda, K., Shuman, H., Rodionov, V., Ikebe, M., Goldman, Y.E., and Holzbaur, E.L. (2012). Force-dependent detachment of kinesin-2 biases track switching at cytoskeletal filament intersections. Biophys. J. *103*, 48–58.
15. Brunnbauer, M., Mueller-Planitz, F., Kösem, S., Ho, T.H., Dombi, R., Gebhardt, J.C., Rief, M., and Okten, Z. (2010). Regulation of a heterodimeric kinesin-2 through an unprocessive motor domain that is turned processive by its partner. Proc. Natl. Acad. Sci. USA *107*, 10460–10465.
16. Shastry, S., and Hancock, W.O. (2010). Neck linker length determines the degree of processivity in kinesin-1 and kinesin-2 motors. Curr. Biol. *20*, 939–943.
17. Muthukrishnan, G., Zhang, Y., Shastry, S., and Hancock, W.O. (2009). The processivity of kinesin-2 motors suggests diminished front-head gating. Curr. Biol. *19*, 442–447.
18. Hendricks, A.G., Perlson, E., Ross, J.L., Schroeder, H.W., III, Tokito, M., and Holzbaur, E.L. (2010). Motor coordination via a tug-of-war mechanism drives bidirectional vesicle transport. Curr. Biol. *20*, 697–702.
19. Jamison, D.K., Driver, J.W., Rogers, A.R., Constantinou, P.E., and Diehl, M.R. (2010). Two kinesins transport cargo primarily via the action of one motor: implications for intracellular transport. Biophys. J. *99*, 2967–2977.
20. Soppina, V., Rai, A.K., Ramaiya, A.J., Barak, P., and Mallik, R. (2009). Tug-of-war between dissimilar teams of microtubule motors regulates transport and fission of endosomes. Proc. Natl. Acad. Sci. USA *106*, 19381–19386.
21. Driver, J.W., Jamison, D.K., Uppulury, K., Rogers, A.R., Kolomeisky, A.B., and Diehl, M.R. (2011). Productive cooperation among processive motors depends inversely on their mechanochemical efficiency. Biophys. J. *101*, 386–395.
22. Müller, M.J., Klumpp, S., and Lipowsky, R. (2008). Tug-of-war as a cooperative mechanism for bidirectional cargo transport by molecular motors. Proc. Natl. Acad. Sci. USA *105*, 4609–4614.
23. Kunwar, A., Tripathy, S.K., Xu, J., Mattson, M.K., Anand, P., Sigua, R., Vershinin, M., McKenney, R.J., Yu, C.C., Mogilner, A., and Gross, S.P. (2011). Mechanical stochastic tug-of-war models cannot explain bidirectional lipid-droplet transport. Proc. Natl. Acad. Sci. USA *108*, 18960–18965.
24. Rosenfeld, S.S., Fordyce, P.M., Jefferson, G.M., King, P.H., and Block, S.M. (2003). Stepping and stretching. How kinesin uses internal strain to walk processively. J. Biol. Chem. *278*, 18550–18556.
25. Block, S.M., Goldstein, L.S., and Schnapp, B.J. (1990). Bead movement by single kinesin molecules studied with optical tweezers. Nature *348*, 348–352.
26. Kaan, H.Y., Hackney, D.D., and Kozielski, F. (2011). The structure of the kinesin-1 motor-tail complex reveals the mechanism of autoinhibition. Science *333*, 883–885.
27. Hammond, J.W., Blasius, T.L., Soppina, V., Cai, D., and Verhey, K.J. (2010). Autoinhibition of the kinesin-2 motor KIF17 via dual intramolecular mechanisms. J. Cell Biol. *189*, 1013–1025.
28. Visscher, K., Schnitzer, M.J., and Block, S.M. (1999). Single kinesin molecules studied with a molecular force clamp. Nature *400*, 184–189.
29. Schnitzer, M.J., and Block, S.M. (1997). Kinesin hydrolyses one ATP per 8-nm step. Nature *388*, 386–390.

30. Milic, B., Andreasson, J.O.L., Hancock, W.O., and Block, S.M. (2014). Kinesin processivity is gated by phosphate release. Proc. Natl. Acad. Sci. USA *111*, 14136–14140.

31. Clancy, B.E., Behnke-Parks, W.M., Andreasson, J.O., Rosenfeld, S.S., and Block, S.M. (2011). A universal pathway for kinesin stepping. Nat. Struct. Mol. Biol. *18*, 1020–1027.

32. Johnson, K.A., Simpson, Z.B., and Blom, T. (2009). FitSpace Explorer: an algorithm to evaluate multidimensional parameter space in fitting kinetic data. Anal. Biochem. *387*, 30–41.

33. Uemura, S., Kawaguchi, K., Yajima, J., Edamatsu, M., Toyoshima, Y.Y., and Ishiwata, S. (2002). Kinesin-microtubule binding depends on both nucleotide state and loading direction. Proc. Natl. Acad. Sci. USA *99*, 5977–5981.

34. Shastry, S., and Hancock, W.O. (2011). Interhead tension determines processivity across diverse N-terminal kinesins. Proc. Natl. Acad. Sci. USA *108*, 16253–16258.

35. Bell, G.I. (1978). Models for the specific adhesion of cells to cells. Science *200*, 618–627.

36. Hwang, W., Lang, M.J., and Karplus, M. (2008). Force generation in kinesin hinges on cover-neck bundle formation. Structure *16*, 62–71.

37. Okada, Y., and Hirokawa, N. (2000). Mechanism of the single-headed processivity: diffusional anchoring between the K-loop of kinesin and the C terminus of tubulin. Proc. Natl. Acad. Sci. USA *97*, 640–645.

38. Thorn, K.S., Ubersax, J.A., and Vale, R.D. (2000). Engineering the processive run length of the kinesin motor. J. Cell Biol. *151*, 1093–1100.

39. Tuma, M.C., Zill, A., Le Bot, N., Vernos, I., and Gelfand, V. (1998). Heterotrimeric kinesin II is the microtubule motor protein responsible for pigment dispersion in *Xenopus* melanophores. J. Cell Biol. *143*, 1547–1558.

40. Valentine, M.T., Guydosh, N.R., Gutiérrez-Medina, B., Fehr, A.N., Andreasson, J.O., and Block, S.M. (2008). Precision steering of an optical trap by electro-optic deflection. Opt. Lett. *33*, 599–601.

41. Chemla, Y.R., Moffitt, J.R., and Bustamante, C. (2008). Exact solutions for kinetic models of macromolecular dynamics. J. Phys. Chem. B *112*, 6025–6044.

Current Biology

Supplemental Information

The Mechanochemical Cycle of Mammalian Kinesin-2 KIF3A/B under Load

Johan O.L. Andreasson, Shankar Shastry, William O. Hancock, and Steven M. Block

Supplemental Figures

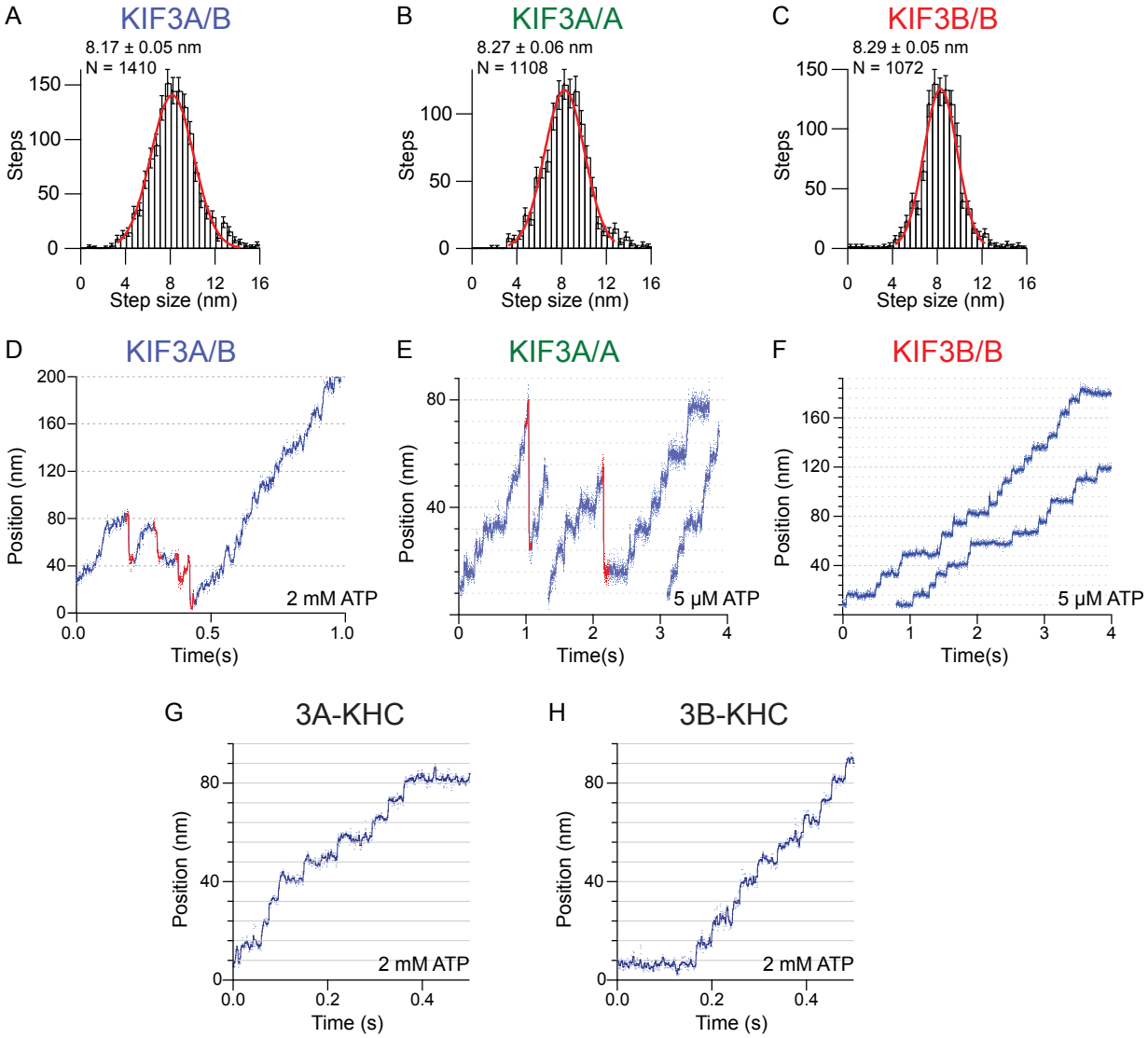

Figure S1, Related to Figure 1. (A-C) Histograms of the step-size distribution of forward steps for KIF3A/B, KIF3A/A, and KIF3B/B under hindering load (5 µM ATP, 4 pN, error bars indicate s.d.), with single gaussian fits (solid red lines; means, s.e., and *N* are supplied in the legends). (D-H) Representative single-molecule records for the indicated kinesin constructs, subject to hindering loads applied by an optical force clamp, and displaying individual steps. Raw data and median-filtered traces are superposed (blue); rearward slips are indicated (red). (D) KIF3A/B (2 mM ATP, 4 pN hindering load). (E-F) KIF3A/A and KIF3B/B (5 µM ATP, 4 pN hindering load). (G-H) 3A-KHC and 3B-KHC (2 mM ATP, 5 pN hindering load).

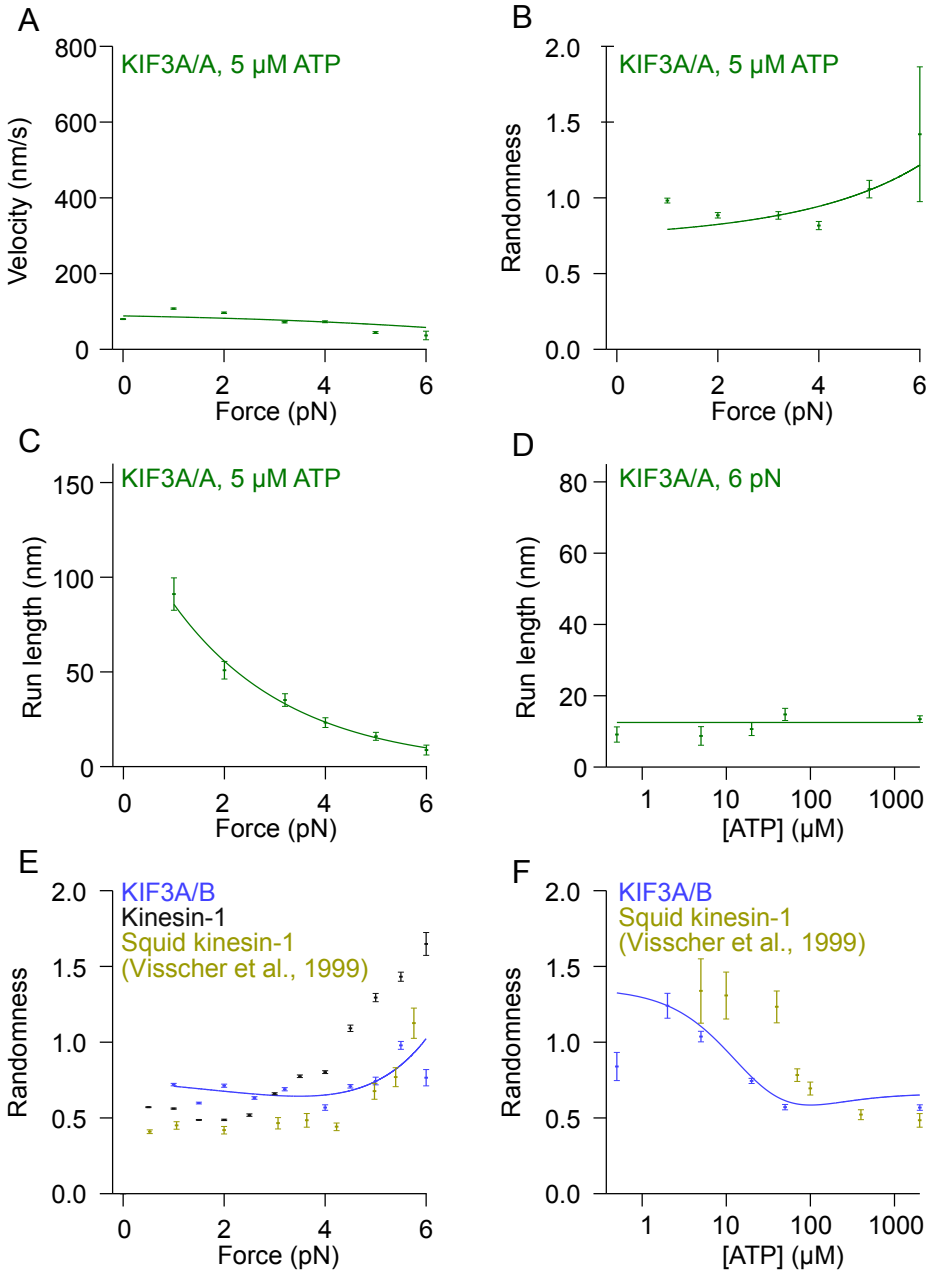

Figure S2, Related to Figure 2 and 4. A, B. KIF3A/A velocity and randomness as a function of hindering load (mean ± s.e.; 5 µM ATP). Curves (solid lines) are from the global fit shown in Figure 2. C. KIF3A/A run length as a function of hindering load (mean ± s.e., at 5 µM ATP). The curve (solid line) shows an exponential fit (L_0 = 132 ± 13 nm, δ = 1.8 ± 0.1 nm). D. KIF3A/A run length as a function of ATP concentration (mean ± s.e., at 6 pN hindering load). The data are fit to a constant (12.5 ± 0.7 nm, solid line). E. Randomness for KIF3A/B as a function of load (blue dots, mean ± s.e., 2 mM ATP). The curve (blue, solid line) shows the global fit. Plotted for comparison are randomness data for *Drosophila* kinesin-1 (dark grey points, mean ± s.e., data from this study) and squid kinesin-1 (olive dots, mean ± s.e., data from [S1]). F. Randomness for KIF3A/B as a function of ATP concentration (blue dots, mean ± s.e., 4 pN hindering load), compared to squid kinesin-1 (3.59 pN hindering load, olive dots, mean ± s.e., data from [S1]).

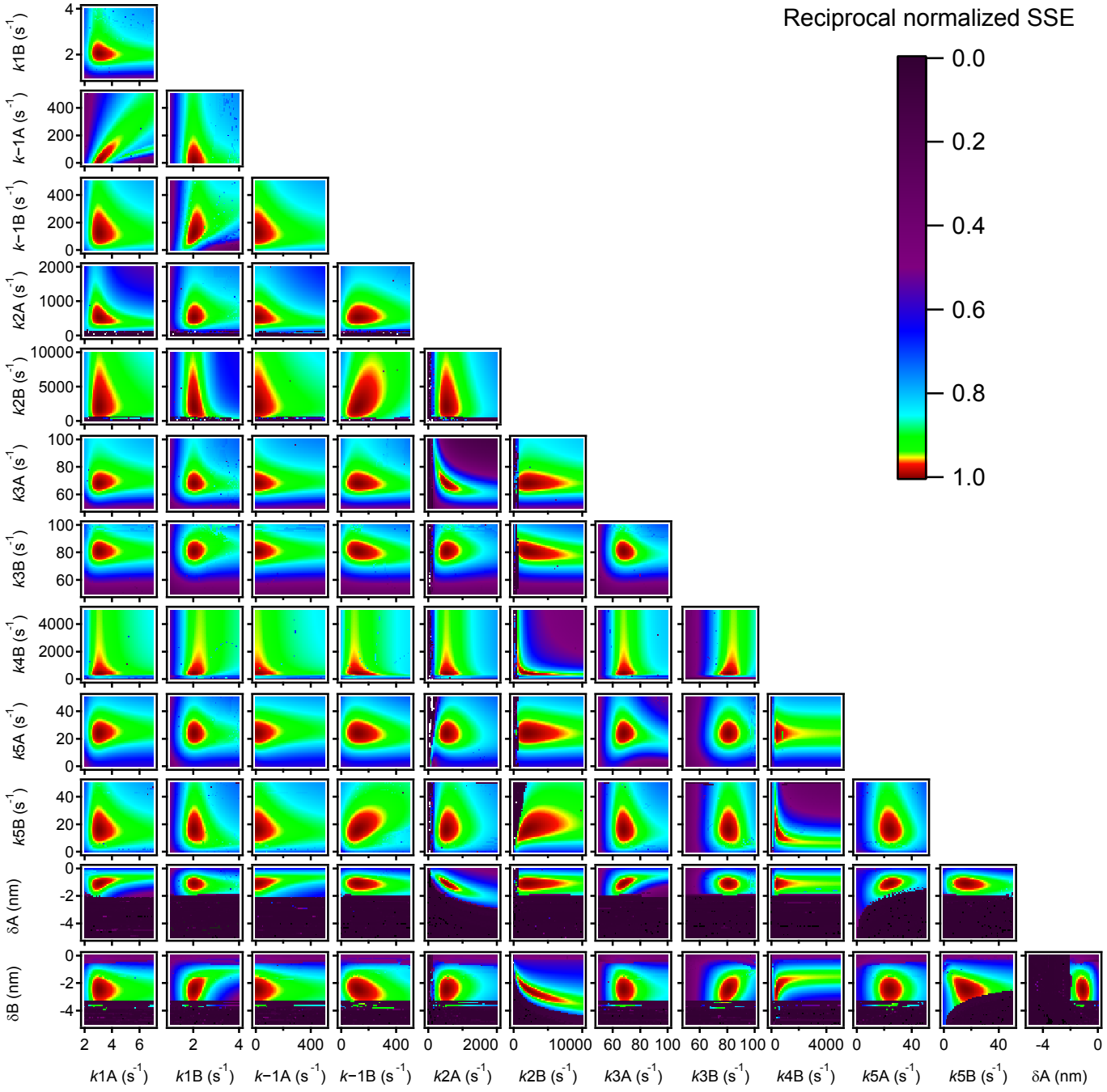

Figure S3, Related to Figure 3**.** Two-dimensional representations of FitSpace contours of the reciprocal normalized SSE values (Sum Square Errors, see Supplemental Experimental Procedures), showing the stability and goodness-of-fit of the model. Parameter names are those for the model described in Supplemental Experimental Procedures (below). Sharps peaks (dark red color) indicate stable convergence of the fit to a narrow range of the parameter values; regions of non-convergence are indicated by black.

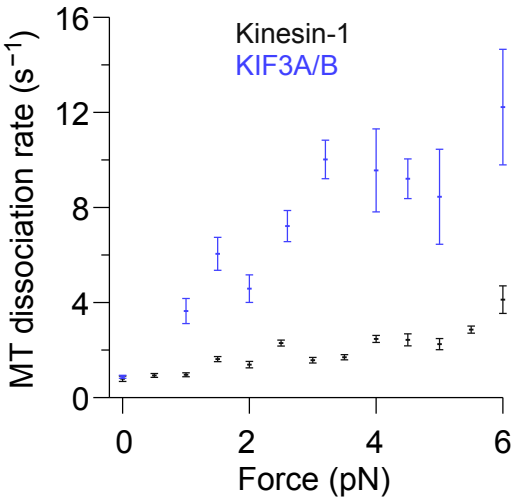

Figure S4, Related to Figure 5. Force dependence of the dissociation rate from the microtubule during processive stepping by KIF3A/B (blue dashes; mean ± s.e.), compared to kinesin-1 (dark grey dashes; mean ± s.e.). Dissociation rates were calculated by dividing the velocity by the run length, using the data of Figs. 2 and 4 (main text).

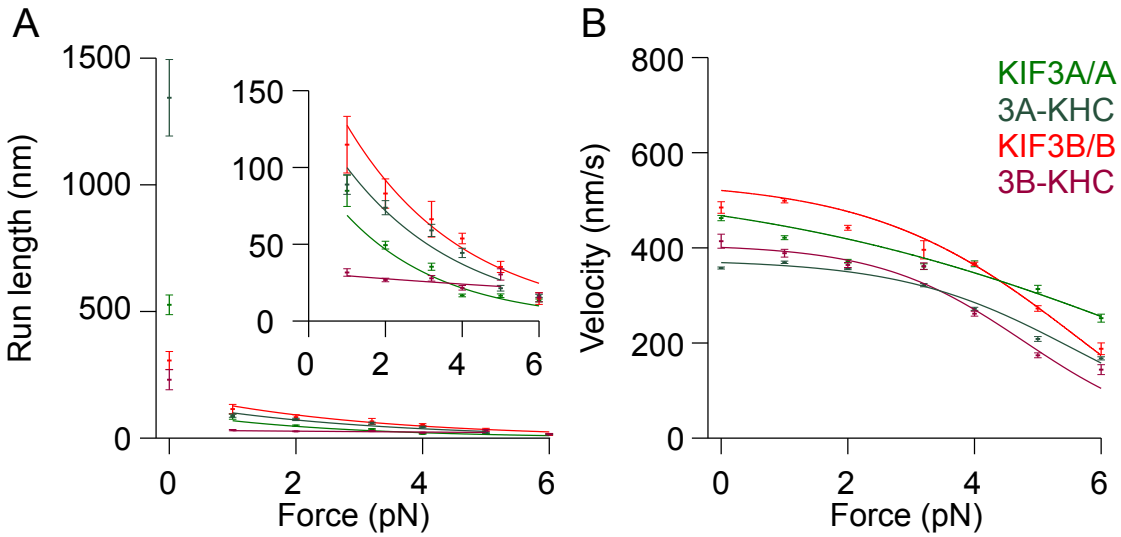

Figure S5, related to Figure 6. Comparison between homodimeric constructs with the native KIF3A/B stalk (KIF3A/A, KIF3B/B) and with the kinesin-1 stalk (3A-KHC, 3B-KHC). A. Run length as a function of force (dashes; mean ± s.e., color code in legend). Inset: Expanded view at non-zero loads. Fits to exponential functions (solid lines) with the parameters given in Figure 4 and Table S4. B. Velocity as a function of force (dashes; mean ± s.e.). Solid lines are fits to global model (KIF3A/A, KIF3B/B) or the 3-state model of Table S1 (3A-KHC, 3B-KHC).

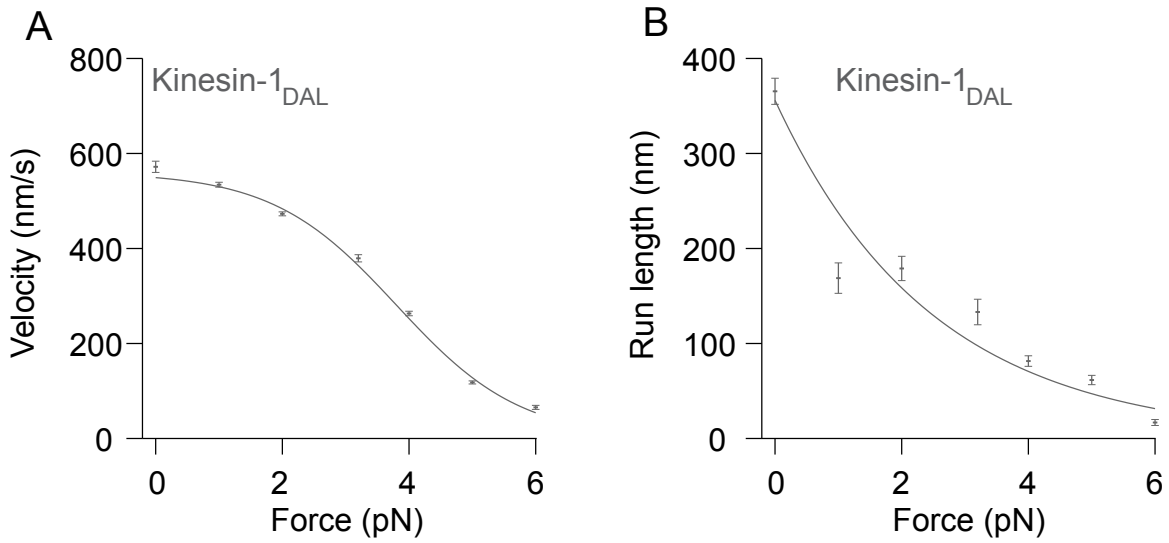

Figure S6, related to Figure 6. Kinesin-1_{DAL} velocity and run length as functions of load. A. Kinesin-1_{DAL} velocity vs. force at saturating ATP concentration (2 mM; dashes; mean ± s.e.). Data were fit to a 3-state model (solid grey curve, parameters in Table S1). B. Kinesin-1_{DAL} run length vs. force at saturating ATP concentration (2 mM; dashes; mean ± s.e.). Data were fit to an exponential, with unloaded run length L_o = 356 ± 12 nm and distance parameter δ = 1.64 ± 0.05 nm.

Supplemental Tables

Table S1, related to Figures 2A and S5. Kinetic parameters (fit parameters ± s.e. from fit) for the processive stepping of kinesin-1 and kinesin-1_{DAL}. The experimental force-velocity curve for kinesin-1 in Figure 2A and for kinesin-1_{DAL} in Figure S5, obtained in 2 mM ATP, were fit to the following kinetic scheme:

$$[1] \xleftrightarrow{k_1\,[\mathrm{ATP}]/\,k_{-1}} [2] \xrightarrow{k_2 \exp\left(-\frac{F\delta}{k_B T}\right)} [3] \xrightarrow{k_3} [1]$$

The scheme is similar to that in Figure 3. The rates k_3 and k_4 in Figure 3 have been combined into k_3 here, and the back-stepping pathway was not included. Because ATP binding is fast under saturating ATP conditions, the second order ATP binding rate, k_1=3 μM^{-1} s^{-1} , and ATP unbinding rate, k_{-1}=50 s^{-1}, were taken to be fixed.

Rate	Transition	kinesin-1	kinesin-1_{DAL}
k_2	Neck-linker docking (s^{-1})	2753 ± 163	3311 ± 467
k_3	ATP hydrolysis (s^{-1})	98.9 ± 0.5	69.2 ± 0.9
δ	Distance parameter (nm)	3.58 ± 0.05	4.13 ± 0.12

Table S2, Confidence intervals for the parameters in the kinetic model. The cited fit values represent the best fit, and the fit errors are the associated least-square fit errors. The lower and upper limits were derived from FitSpace contours at the 5% sum square error (SSE) level (see Supplemental Experimental Procedures). All rate constants have units of s^{-1}, and the distance parameters (δ) has units of nm.

	Least-squares fit parameters		FitSpace analysis confidence intervals	
Parameter	**Fit value**	**Fit error**	**Lower limit**	**Upper limit**
k_{1A}	3.06	0.06	2.5	4.9
k_{1B}	2.06	0.03	1.7	2.8
k_{-1A}	12	7	0	160
k_{-1B}	124	10	42	330
k_{2A}	530	21	310	970
k_{2B}	1,730	211	510	7,900
k_{3A}	67.9	0.5	62	86
k_{3B}	81.2	0.6	74	99
k_{4A}	50000 (fixed)	N/A	670	N/A
k_{4B}	439	26	270	2,100
k_{5A}	23.5	0.7	17	38
k_{5B}	17	1	6.9	34
δ_A	1.09	0.04	0.63	1.8
δ_B	2.28	0.09	1.5	3.7

Table S3, related to Figure 6B. Kinetic parameters for the processive stepping of kinesin-2 mutants. The experimental force-velocity curve for the kinesin-2 mutants in Figure 6B, obtained in 2 mM ATP, were fit to the kinetic scheme described in the caption of Table S1:

Kinetic parameters for kinesin-2 mutants

Rate	Transition	3A-KHC	3A-KHC$_{P>A}$	3A-KHC$_{P>A, \Delta DAL}$	3B-KHC
k_2	Neck-linker docking (s^{-1})	2,800 ± 400	1,300 ± 300	800 ± 100	3,200 ± 1,000
k_3	ATP hydrolysis (s^{-1})	46.1 ± 0.3	47.6 ± 0.8	48.7 ± 0.7	50 ± 1
δ	Distance parameter (nm)	3.0 ± 0.1	2.1 ± 0.2	2.1 ± 0.1	3.5 ± 0.3

Table S4. Run length parameters for kinesin-2 mutants. L_{obs} is the observed (measured) unloaded run length using video centroid tracking; L_0 is the unloaded run length extrapolated from exponential fits to the run length data obtained under load.

Run length parameters for kinesin-2 mutants

Rate	Transition	3A-KHC	3A-KHC$_{P>A}$	3A-KHC$_{P>A, \Delta DAL}$	3B-KHC
L_{obs}	Unloaded run length (nm)	1,344 ± 151	893 ± 95	2,855 ± 299	231 ± 40
L_0	Extrapolated run length (nm)	139 ± 10	119 ± 8	115 ± 12	32 ± 2
δ	Distance parameter (nm)	1.3 ± 0.1	1.6 ± 0.1	1.4 ± 0.1	0.3 ± 0.1

Supplemental Experimental Procedures

Expressions for fit to kinetic model

Individual terms from a 7-by-7 matrix determinant were combined to obtain velocity and randomness expressions that were subsequently exported to IGOR Pro (Wavemetrics) for fitting purposes. The velocity and randomness data, as function of force (*F*) and ATP (*T*), were fit to the expressions given below. In the fitting procedure, hindering loads corresponded to negative force values. Similarly, characteristic distance parameters measured under hindering loads take on negative distance values.

Velocity(F, T)= vel1/(vel2+vel3) and
Randomess(F, T)=ddgamma/dgamma-2*dbeta/beta+2*alpha*dgamma/(beta^2)

where d=8.2, kT=4.056, d5a=0, d5b=0, d6a=0, d6b=0, k4a=50000 and

vel1=(2*T*d*k1a*k1b*k3a*k3b*k4a*k4b*(exp(((d2a+d5a)*F)/kT)*k2b*k5a+exp(((d2a+d2b+d5a+d5b)*F)/kT)*k5a*k5b+k2a*(k2b+exp(((d2b+d5b)*F)/kT)*k5b)-exp(((d2a+d2b+d6a+d6b)*F)/kT)*k6a*k6b))

vel21=exp((d2b*F)/kT)*k1a*k1mb*k2a+exp((d2a*F)/kT)*k1b*k1ma*k2b+(k1a+k1b)*k2a*k2b+exp(((d2a+d2b+d5a)*F)/kT)*k1a*k1mb*k5a+exp(((d2a+d5a)*F)/kT)*(k1a+k1b)*k2b*k5a+exp(((d2a+d2b+d5b)*F)/kT)*k1b*k1ma*k5b

vel22=exp(((d2b+d5b)*F)/kT)*(k1a+k1b)*k2a*k5b+exp(((d2a+d2b+d5a+d5b)*F)/kT)*(k1a+k1b)*k5a*k5b+exp(((d2a+d2b+d6a)*F)/kT)*k1a*k1mb*k6a+exp(((d2a+d6a)*F)/kT)*(k1a+k1b)*k2b*k6a+exp(((d2a+d2b+d5b+d6a)*F)/kT)*(k1a+k1b)*k5b*k6a

vel23=exp(((d2a+d2b+d6b)*F)/kT)*k1b*k1ma*k6b+exp(((d2b+d6b)*F)/kT)*(k1a+k1b)*k2a*k6b+exp(((d2a+d2b+d5a+d6b)*F)/kT)*(k1a+k1b)*k5a*k6b+exp(((d2a+d2b+d6a+d6b)*F)/kT)*(k1a+k1b)*k6a*k6b

vel2=k3a*k3b*k4a*k4b*(vel21+vel22+vel23)

vel31=exp((d2a*F)/kT)*k2b*k3b*k4a*k4b+exp(((d2a+d2b+d5a)*F)/kT)*k3b*k4a*k4b*k5a+exp(((d2a+d5a)*F)/kT)*k2b*(k4a*k4b+k3b*(k4a+k4b))*k5a+exp(((d2a+d2b+d5b)*F)/kT)*k3b*k4a*k4b*k5b

vel32=exp(((d2a+d2b+d5a+d5b)*F)/kT)*k3b*(k4a+k4b)*k5a*k5b+exp(((d2a+d2b+d6a)*F)/kT)*k3b*k4a*k4b*k6a+exp(((d2a+d6a)*F)/kT)*k2b*k4a*(k3b+k4b)*k6a

vel325=exp(((d2a+d2b+d5b+d6a)*F)/kT)*k3b*k4a*k5b*k6a+exp(((d2a+d2b+d6b)*F)/kT)*k3b*k4a*k4b*k6b+exp(((d2a+d2b+d5a+d6b)*F)/kT)*k3b*k4b*k5a*k6b

vel33=k2a*(k2b*(k3a*k3b*k4a+k3b*k4a*k4b+k3a*(k3b+k4a)*k4b)+k3b*(exp((d2b*F)/kT)*k3a*k4a*k4b+exp(((d2b+d5b)*F)/kT)*(k3a*k4a+(k3a+k4a)*k4b)*k5b+exp(((d2b+d6b)*F)/kT)*(k3a+k4a)*k4b*k6b)

vel3=T*k1a*k1b*(k3a*(vel31+vel32+vel325)+vel33)

beta11=exp((d2b*F)/kT)*k1a*k1mb*k2a+exp((d2a*F)/kT)*k1b*k1ma*k2b+(k1a+k1b)*k2a*k2b+exp(((d2a+d2b+d5a)*F)/kT)*k1a*k1mb*k5a+exp(((d2a+d5a)*F)/kT)*(k1a+k1b)*k2b*k5a

beta12=exp(((d2a+d2b+d5b)*F)/kT)*k1b*k1ma*k5b+exp(((d2b+d5b)*F)/kT)*(k1a+k1b)*k2a*k5b+exp(((d2a+d2b+d5a+d5b)*F)/kT)*(k1a+k1b)*k5a*k5b+exp(((d2a+d2b+d6a)*F)/kT)*k1a*k1mb*k6a

beta13=exp(((d2a+d6a)*F)/kT)*(k1a+k1b)*k2b*k6a+exp(((d2a+d2b+d5b+d6a)*F)/kT)*(k1a+k1b)*k5b*k6a+exp(((d2a+d2b+d6b)*F)/kT)*k1b*k1ma*k6b

beta14=exp(((d2b+d6b)*F)/kT)*(k1a+k1b)*k2a*k6b+exp(((d2a+d2b+d5a+d6b)*F)/kT)*(k1a+k1b)*k5a*k6b+exp(((d2a+d2b+d6a+d6b)*F)/kT)*(k1a+k1b)*k6a*k6b

beta1=k3a*k3b*k4a*k4b*(beta11+beta12+beta13+beta14)

beta21=exp((d2a*F)/kT)*k2b*k3b*k4a*k4b+exp(((d2a+d2b+d5a)*F)/kT)*k3b*k4a*k4b*k5a+exp(((d2a+d5a)*F)/kT)*k2b*(k4a*k4b+k3b*(k4a+k4b))*k5a+exp(((d2a+d2b+d5b)*F)/kT)*k3b*k4a*k4b*k5b

beta22=exp(((d2a+d2b+d5a+d5b)*F)/kT)*k3b*(k4a+k4b)*k5a*k5b+exp(((d2a+d2b+d6a)*F)/kT)*k3b*k4a*k4b*k6a+exp(((d2a+d6a)*F)/kT)*k2b*k4a*(k3b+k4b)*k6a

beta23=exp(((d2a+d2b+d5b+d6a)*F)/kT)*k3b*k4a*k5b*k6a+exp(((d2a+d2b+d6b)*F)/kT)*k3b*k4a*k4b*k6b+exp(((d2a+d2b+d5a+d6b)*F)/kT)*k3b*k4b*k5a*k6b

beta24=k2b*(k3a*k3b*k4a+k3b*k4a*k4b+k3a*(k3b+k4a)*k4b)+k3b*(exp((d2b*F)/kT)*k3a*k4a*k4b+exp(((d2b+d5b)*F)/kT)*(k3a*k4a+(k3a+k4a)*k4b)*k5b+exp(((d2b+d6b)*F)/kT)*(k3a+k4a)*k4b*k6b)

beta2=T*k1a*k1b*(k3a*(beta21+beta22+beta23)+k2a*beta24)

beta=T*exp(-(((d2a+d2b)*F)/kT))*(beta1+beta2)

dgamma=-2*T^2*exp(-(((d2a+d2b)*F)/kT))*k1a*k1b*k3a*k3b*k4a*k4b*(exp(((d2a+d5a)*F)/kT)*k2b*k5a+exp(((d2a+d2b+d5a+d5b)*F)/kT)*k5a*k5b+k2a*(k2b+exp(((d2b+d5b)*F)/kT)*k5b)-exp(((d2a+d2b+d6a+d6b)*F)/kT)*k6a*k6b)

ddgamma=-4*T^2*exp(-(((d2a+d2b)*F)/kT))*k1a*k1b*k3a*k3b*k4a*k4b*(exp(((d2a+d5a)*F)/kT)*k2b*k5a+exp(((d2a+d2b+d5a+d5b)*F)/kT)*k5a*k5b+k2a*(k2b+exp(((d2b+d5b)*F)/kT)*k5b)+exp(((d2a+d2b+d6a+d6b)*F)/kT)*k6a*k6b)

dbeta=-2*T^2*exp(-(((d2a+d2b)*F)/kT))*k1a*k1b*(k4a*k4b*(exp(((d2a+d5a)*F)/kT)*k2b*k3b*k5a+exp(((d2b+d5b)*F)/kT)*k2a*k3a*k5b+exp(((d2a+d2b+d5a+d5b)*F)/kT)*(k3a+k3b)*k5a*k5b)-exp(((d2a+d2b+d6a+d6b)*F)/kT)*(k3a*k3b*k4a+k3b*k4a*k4b+k3a*(k3b+k4a)*k4b)*k6a*k6b)

alpha11=exp(((d2a+d2b)*F)/kT)*(k1b*k1ma+k1a*k1mb)*k3a*k3b*k4a*k4b+(k1a+k1b)*k2a*k2b*(k3a*k3b*k4a+k3b*k4a*k4b+k3a*(k3b+k4a)*k4b)

alpha12=exp((d2a*F)/kT)*k2b*(k1b*k1ma*k3a*k3b*k4a+k1a*k3a*k3b*k4a*k4b+k1b*(k1ma*k3a*k3b+k3a*k3b*k4a+k1ma*(k3a+k3b)*k4a)*k4b)

alpha13=exp((d2b*F)/kT)*k2a*(k1a*k1mb*k3a*k3b*k4a+k1b*k3a*k3b*k4a*k4b+k1a*(k1mb*k3a*k3b+k3a*k3b*k4a+k1mb*(k3a+k3b)*k4a)*k4b)

alpha14=exp(((d2a+d5a)*F)/kT)*(k1a+k1b)*k2b*(k3a*k3b*k4a+k3b*k4a*k4b+k3a*(k3b+k4a)*k4b)*k5a

alpha15=exp(((d2a+d2b+d5a)*F)/kT)*(k1a*k1mb*k3a*k3b*k4a+k1b*k3a*k3b*k4a*k4b+k1a*(k1mb*k3a*k3b+k3a*k3b*k4a+k1mb*(k3a+k3b)*k4a)*k4b)*k5a

alpha16=exp(((d2b+d5b)*F)/kT)*(k1a+k1b)*k2a*(k3a*k3b*k4a+k3b*k4a*k4b+k3a*(k3b+k4a)*k4b)*k5b

alpha17=exp(((d2a+d2b+d5b)*F)/kT)*(k1b*k1ma*k3a*k3b*k4a+k1a*k3a*k3b*k4a*k4b+k1b*(k1ma*k3a*k3b+k3a*k3b*k4a+k1ma*(k3a+k3b)*k4a)*k4b)*k5b

alpha18=exp(((d2a+d2b+d5a+d5b)*F)/kT)*(k1a+k1b)*(k3a*k3b*k4a+k3b*k4a*k4b+k3a*(k3b+k4a)*k4b)*k5a*k5b+exp(((d2a+d6a)*F)/kT)*(k1a+k1b)*k2b*(k3a*k3b*k4a+k3b*k4a*k4b+k3a*(k3b+k4a)*k4b)*k6a

alpha19=exp(((d2a+d2b+d6a)*F)/kT)*(k1a*k1mb*k3a*k3b*k4a+k1b*k3a*k3b*k4a*k4b+k1a*(k1mb*k3a*k3b+k3a*k3b*k4a+k1mb*(k3a+k3b)*k4a)*k4b)*k6a

alpha20=exp(((d2a+d2b+d5b+d6a)*F)/kT)*(k1a+k1b)*(k3a*k3b*k4a+k3b*k4a*k4b+k3a*(k3b+k4a)*k4b)*k5b*k6a+exp(((d2b+d6b)*F)/kT)*(k1a+k1b)*k2a*(k3a*k3b*k4a+k3b*k4a*k4b+k3a*(k3b+k4a)*k4b)*k`b

alpha21=exp(((d2a+d2b+d6b)*F)/kT)*(k1b*k1ma*k3a*k3b*k4a+k1a*k3a*k3b*k4a*k4b+k1b*(k1ma*k3a*k3b+k3a*k3b*k4a+k1ma*(k3a+k3b)*k4a)*k4b)*k6b

alpha22=exp(((d2a+d2b+d5a+d6b)*F)/kT)*(k1a+k1b)*(k3a*k3b*k4a+k3b*k4a*k4b+k3a*(k3b+k4a)*k4b)*k5a*k6b+exp(((d2a+d2b+d6a+d6b)*F)/kT)*(k1a+k1b)*(k3a*k3b*k4a+k3b*k4a*k4b+k3a*(k3b+k4a)*k4b)*k6a*k6b

alpha23=k3a*k3b*k4a*k4b*(k2a+exp((d2a*F)/kT)*(k1ma+exp((d5a*F)/kT)*k5a+exp((d6a*F)/kT)*k6a))*(k2b+exp((d2b*F)/kT)*(k1mb+exp((d5b*F)/kT)*k5b+exp((d6b*F)/kT)*k6b))

alpha30=exp(((d2a+d2b)*F)/kT)*k3a*k3b*k4a*k4b+exp((d2a*F)/kT)*k2b*(k3a*k3b*k4a+k3b*k4a*k4b+k3a*(k3b+k4a)*k4b)
+exp(((d2a+d2b+d5a)*F)/kT)*(k3a*k3b*k4a+k3b*k4a*k4b+k3a*(k3b+k4a)*k4b)*k5a

alpha31=exp(((d2a+d5a)*F)/kT)*k2b*(k4a*k4b+k3b*(k4a+k4b)+k3a*(k3b+k4a+k4b))*k5a+exp(((d2a+d2b+d5b)*F)/kT)*(k3a*
k3b*k4a+k3b*k4a*k4b+k3a*(k3b+k4a)*k4b)*k5b

alpha32=exp(((d2a+d2b+d5a+d5b)*F)/kT)*(k3b*(k4a+k4b)+k3a*(k3b+k4a+k4b))*k5a*k5b+exp(((d2a+d2b+d6a)*F)/kT)*(k3a*
k3b*k4a+k3b*k4a*k4b+k3a*(k3b+k4a)*k4b)*k6a

alpha33=exp(((d2a+d6a)*F)/kT)*k2b*(k4a*(k3b+k4b)+k3a*(k3b+k4a+k4b))*k6a+exp(((d2a+d2b+d5b+d6a)*F)/kT)*(k3b*k4a+
k3a*(k3b+k4a))*k5b*k6a

alpha34=exp(((d2a+d2b+d6b)*F)/kT)*(k3a*k3b*k4a+k3b*k4a*k4b+k3a*(k3b+k4a)*k4b)*k6b+exp(((d2a+d2b+d5a+d6b)*F)/k
T)*(k3b*k4b+k3a*(k3b+k4b))*k5a*k6b

alpha35=k2a*(exp((d2b*F)/kT)*(k3a*k3b*k4a+k3b*k4a*k4b+k3a*(k3b+k4a)*k4b)+k2b*(k3b*k4a+(k3b+k4a)*k4b+k3a*(k3b+
k4a+k4b))+exp(((d2b+d5b)*F)/kT)*(k3b*k4a+(k3b+k4a)*k4b+k3a*(k3b+k4a+k4b))*k5b+exp(((d2b+d6b)*F)/kT)*(k3b*(k3a+k
4a)+(k3a+k3b+k4a)*k4b)*k6b)

alpha=exp(-(((d2a+d2b)*F)/kT))*(T*(alpha11+alpha12+alpha13+alpha14+alpha15+alpha16+alpha17+
alpha18+alpha19+alpha20+alpha21+alpha22)+alpha23+T^2*k1a*k1b*(alpha30+alpha31+alpha32+alpha33+alpha34+alpha35))

FitSpace Explorer Error Analysis

Confidence contours were calculated for all pairs of parameters in the kinetic model, based on the method of Johnson et al. [S2]. The sum square error (SSE) was calculated for the optimal values from the fit. Then, new fits were calculated by fixing the parameter pair (here, denoted as x and y) while letting all other parameters vary. Two-dimensional views of the contours of the reciprocal normalized SSE ($SSEmin/SSE_{x,y}$) were plotted over appropriate ranges of x and y (Figure S3). Confidence intervals were calculated at the 5% level by iteratively calculating contours around the minimum and maximum values of x and y where $SSEmin/SSE_{x,y} = 1/1.05$ (Table S2).The FitSpace analysis confirms that the parameter set is properly constrained by the experimental data, as the contours are generally well-defined for each pair. Both the FitSpace analysis and the error from the least-squares fit depend on the experimental errors, which for all velocities were represented as the standard error of the mean (s.e.m.). For many experimental conditions, the errors were small, due to the large number of data points, and other systematic sources of error may dominate. The FitSpace analysis highlights any interdependencies between parameters, and helps determine confidence in the model. The lower and upper limits indicate that the confidence intervals from this analysis are generally wider than those obtained from the least squares fit, and may better represent the accuracy of the model.

The parameters associated with ATP binding and hydrolysis ($k_{1A,B}$ and $k_{3A,B}$) and the distance parameters (δ) were more narrowly determined than those of ATP unbinding ($k_{-1A,B}$) and neck linker docking ($k_{2A,B}$). The interval was wide for P_i release (k_{4B}) at the 5% level, and we found that the contour could not be determined at the 10% level. The inverse of the randomness represents the number of rate-limiting steps in a linear cycle and at low forces, k_{2B} and k_{4B} are expected to be rate-limiting for the KIF3B head. Their interdependence is evident from the contour plot. Because k_{4b} represents a biochemical step that is solely determined from the randomness data, it is natural that this parameter is the least constrained. The corresponding parameter for the KIF3A head, k_{4A}, could not be constrained due to the high randomness values of KIF3A constructs, and was therefore included in the fit only as a fixed (very fast) parameter.

Supplemental References

S1. Visscher, K., Schnitzer, M.J., and Block, S.M. (1999). Single kinesin molecules studied with a molecular force clamp. Nature 400, 184-189.

S2. Johnson, K.A., Simpson, Z.B., and Blom, T. (2009). FitSpace explorer: an algorithm to evaluate multidimensional parameter space in fitting kinetic data. Anal Biochem 387, 30-41.